Karlsruher Institut für Technologie

FAKULTÄT FÜR PHYSIK
Institut für Experimentelle Teilchenphysik

Calibration and Monitoring of KATRIN's Precision High Voltage System with First ^{83m}Kr Measurements

Kalibrierung und Überwachung
von KATRINs Präzisionshochspannungssystem
mit ersten ^{83m}Kr-Messungen

Masterarbeit
von

Caroline Rodenbeck

am Institut für Experimentelle Teilchenphysik

Referent:	Prof. Dr. G. Drexlin
Korreferent:	Dr. K. Valerius
Betreuender Mitarbeiter:	Dr. T. Thümmler

Bearbeitungszeit: 15.02.2017 – 15.02.2018

Erklärung zur Selbstständigkeit

Ich versichere, dass ich diese Arbeit selbstständig verfasst habe und keine anderen als die angegebenen Quellen und Hilfsmittel benutzt habe, die wörtlich oder inhaltlich übernommenen Stellen als solche kenntlich gemacht und die Satzung des KIT zur Sicherung guter wissenschaftlicher Praxis in der gültigen Fassung vom 27.11.2014 beachtet habe.

Karlsruhe, den 15.02.2018 ____________________________

Caroline Rodenbeck

Als Ansichtsexemplar genehmigt von

Karlsruhe, den 15.02.2018 ____________________________

Prof. Dr. G. Drexlin

Contents

List of Figures

List of Tables

1 Introduction

At first glance, monitoring voltages is a simple task. Measuring voltages is done by using a voltmeter. The accuracy of the measurement is determined by the quality of the voltmeter. One can go a step further and calibrate the voltmeter to improve the accuracy of the measurement and to ensure reproducible results. However, creating and monitoring voltages of about 18.6 kV with a precision and stability of 3 ppm, as needed for the KATRIN experiment, poses a challenge.

The KATRIN experiment (Angrik et al. 2005) aims to measure the effective mass of the electron antineutrino with a sensitivity of $m(\nu_e) < 0.2\,\mathrm{eV}$. Since the postulation of the neutrinos (Pauli 1930) and their first experimental detection (Cowan et al. 1956), their properties have been the subject of active research. Recent experiments, rewarded with the Nobel Prize in 2015, measured oscillations of neutrino flavor states and – once and for all – proved that neutrinos have a mass (Fukuda et al. 1998; Ahmad et al. 2001).

The absolute mass values of the neutrino flavor states are yet to be determined. KATRIN is a beta decay experiment that investigates the kinematics of weak decays. The kinematics give direct information about the neutrino masses without further requirements.

The heart of the KATRIN experiment is an integrating spectrometer, built to measure electrons from tritium beta decay. The spectrometer uses the MAC-E filter principle (Beamson et al. 1980), combining a magnetic adiabatic guiding field with an electrostatic retarding potential.

Changing the retarding potential in small voltage steps around 18.6 kV measures the endpoint region of the tritium beta decay electron spectrum. This endpoint region contains information about the electron anti-neutrino mass value and will be the focus of neutrino mass measurements with KATRIN.

Measuring the electron neutrino mass with the intended sensitivity requires the energy scale to be stable up to 60 meV. This translates to a stability requirement of 3 ppm for the high voltage system that creates the retarding potential (Angrik et al. 2005). Using customized high voltage power supplies and a dedicated post regulation setup creates a stable voltage that meets the requirement.

To ensure satisfactory performance of the high voltage system and to make energy analysis possible, the voltages need to be measured. This is done by using purpose-built precision high voltage dividers (Thümmler et al. 2009). The scaled voltages are then measured with multimeters that are calibrated with dedicated calibration procedures. Additionally an independent monitoring is performed where the voltages are compared to a nuclear standard. This is done by measuring electron conversion lines from an implanted ^{83m}Kr source at a separate spectrometer (Erhard et al. 2014).

In July 2017 during a commissioning measurement phase with ^{83m}Kr, the first conversion electron spectroscopy with the complete KATRIN beamline was performed (Arenz et al. 2018a). ^{83m}Kr was used in three different forms: gaseous, condensed and implanted. This presented an opportunity for commissioning the complete experimental setup and for testing the high voltage setup under real measurement conditions.

The perfomance of the high voltage system during this commissioning measurement and particularly the monitoring and the dedicated calibration of the high voltage system for future neutrino mass measurements is the focus of this thesis.

2 Neutrino Physics

Neutrinos are elementary particles which are classified as leptons within the standard model of particle physics[1]. They are electrically neutral, they interact via weak interaction and gravity, and they have a mass much smaller than any other known elementary particle (Griffiths 2008). These properties have not been textbook knowledge for a long time and there is still more research being done, in particular the ongoing search for the neutrino mass.

The first part of this chapter recapitulates the history of neutrinos: starting with the postulation of the neutrino, its discovery and the ensuing investigation of its properties, then discussing neutrino sources and finally the discovery of neutrino oscillations. The second part of the chapter gives an overview of the various efforts that aim to measure the neutrino mass and the methods that are employed.

2.1 Neutrino Properties and Their Discovery

Wolfgang Pauli postulated the existence of a particle to explain the continuous energy spectrum of beta decay (Pauli 1930). At that time, beta decay was thought of as the emission of an electron from an atomic nucleus and the simultaneous transformation of that *parent nucleus* into a slightly lighter *daughter nucleus*. Conservation of energy requires the kinetic energy of the emitted electrons to be constant if the parent nuclei are at rest, yet experiments had shown it to vary (cf. pp. 23ff. Griffiths 2008).

Enrico Fermi developed a theory of beta decay which included the postulated particle (Fermi 1934) and named that particle *neutrino*.

It will be shown later that beta decay is not only the cause for the neutrino's postulation, but also an essential ingredient in the measurement of its mass.

The first experimental detection of neutrinos was performed by Cowan and Reines (Cowan et al. 1956). Their experiment made use of inverse beta decay, $\mathrm{p} + \bar{\nu}_\mathrm{e} \longrightarrow \mathrm{n} + \mathrm{e}^+$, having

[1] Initiated by S. Glashow's idea to combine the electromagnetic and weak interactions (Glashow 1961) and developed further by S. Weinbergs "Model of Leptons" (Weinberg 1967) together with A. Salam (Salam 1968). The standard model including the latest physics can be found in the Review of Particle Physics (Patrignani et al. 2016).

protons in a water tank act as targets for the electron-antineutrinos $\bar{\nu}_\mathrm{e}$ emitted by a nuclear reactor. The positron created in the interaction annihilates with an electron, producing two gamma rays which are then detected by means of a scintillator material and a photomultiplier. The neutron created in the interaction is moderated by the water and captured by Cadmium isotopes like ^{113}Cd. This neutron capture creates one or more gamma rays. The coincidence of both gamma ray signals is then used as an indicator for an antineutrino interaction.

In addition to the electron neutrino, two more flavors of neutrino have been observed: the muon neutrino and the tauon neutrino.

The experimental detection of the muon neutrino was performed at the Brookhaven Alternating Gradient Synchrotron (Danby et al. 1962). The discovered neutrinos were produced by pion decay, $\pi \longrightarrow \mu + \nu$. Due to the absence of an electron signal it was deduced that the neutrinos of pion decay are different from those of beta decay.

The DONUT experiment at the Fermilab was the first to detect the neutrino associated with the tauon. Their primary source for the tauon neutrinos was the leptonic decay $D_s \longrightarrow \tau + \bar{\nu}_\tau$ of a D_s meson and the following decay of τ where a ν_τ is created (Kodama et al. 2001).

All three of these initial detections of neutrinos used terrestrial neutrino sources: the first one a nuclear reactor and the other two a particle accelerator. The next subsection will present more neutrino sources.

2.1.1 Neutrino Sources

Terrestrial neutrino sources produce neutrinos with energies ranging from MeV up to 100 GeV. On the lower end of the scale are the reactor neutrinos with energies of 1 MeV to 5 MeV. They are produced by beta decay of fission products: $\mathrm{n} \longrightarrow \mathrm{p} + \mathrm{e}^- + \bar{\nu}_\mathrm{e}$. Every fission produces about 200 MeV and six neutrinos. With the known power of a nuclear reactor the number of produced neutrinos can be predicted.

The predictability of the number of produced neutrinos has been used by the KamLAND experiment to detect neutrinos from another source: the geoneutrinos (Araki et al. 2005). The experiment detected antineutrinos produced by the decay chains of ^{238}U, ^{232}Th and ^{40}K in the earth's mantle and crust.

Another source are particle accelerators: here high-energy protons produced by the accelerator hit a target, whereby pions and kaons are produced. These decay in flight, $\pi^+ \longrightarrow \mu^+ + \nu_\mu$, $\pi^- \longrightarrow \mu^- + \bar{\nu}_\mu$, producing muon neutrinos and muon antineutrinos with energies in the order of GeV. The muons are decelerated and they in turn decay, for example $\mu^- \longrightarrow \mathrm{e}^- + \nu_\mu + \bar{\nu}_\mathrm{e}$, producing electron antineutrinos.

As discussed above, particle accelerators have been used to detect the muon neutrino as well as the tauon neutrino. Another example of an experiment using this type of source is OPERA, which was the first to detect neutrino oscillations in the direct appearance mode of the $\nu_\mu \longrightarrow \nu_\tau$ channel (Agafonova et al. 2015). Neutrino oscillations will be discussed in the subsequent section.

In addition to the category of terrestrial neutrino sources there is the category of astrophysical neutrino sources. Here possible energies range from as little as some μeV up to 10^3 TeV.

Starting at the lower end, there are relic neutrinos of the thermodynamic equilibrium immediately after the big bang. Those thermic neutrinos are now cooled down to about 1.9 K (roughly equal to 112 eV). They played a major role in the early nucleosynthesis of the light elements, for example D, ^{3}He, ^{4}He and others (cf. p. 85, Schmitz 1997).

Solar neutrinos are a neutrino source with energies up to 15 MeV. They are created from the sun's proton–proton chain reaction ($4\,\mathrm{p} \longrightarrow {}^4\mathrm{He} + 2\,\mathrm{e}^+ + 2\,\nu_\mathrm{e}$) and became important in light of the *solar neutrino problem*: different radiochemical experiments starting with the Homestake experiment measured the rate of solar neutrinos and found it to be less than half of what the luminosity of the sun would have suggested (Davis 1964). They measured the solar neutrinos with inverse beta decay in target nuclei: ${}^{A}_{Z}\mathrm{X} + \nu_\mathrm{e} \longrightarrow {}_{Z+1}^{\;\;A}\mathrm{Y} + \mathrm{e}^-$. The daughter nuclei ${}_{Z+1}^{\;\;A}\mathrm{Y}$ were extracted and identified with Auger electrons. The targets, shielded from background in an underground laboratory, were exposed to the solar neutrinos for multiple weeks. The neutrino rate discrepancies were later explained with neutrino oscillations (see 2.1.2).

Neutrinos with slightly larger energies of all three flavors are produced by supernovae. One famous example is the supernova SN1987A in the Large Magellanic Cloud, which is a mini-galaxy at a distance of about 60 kpc from the Milky Way (cf. p. 288 Perkins 2009).

Atmospheric neutrinos with energies up to 10^4 GeV are produced by *secondary cosmic radiation*. Primary cosmic radiation – in the form of protons, for example – interacts with ^{16}O and ^{12}N nuclei in the earth's atmosphere, creating pions and kaons. These then decay in flight into neutrinos and muons, for example: $\pi^+ \longrightarrow \mu^+ + \nu_\mu$, $\mu \longrightarrow \mathrm{e}^+ + \nu_\mathrm{e} + \bar{\nu}_\mu$. One would therefore expect to find twice as many muon neutrinos as electron neutrinos when measuring their numbers. In the 1990s however, different experiments found a muon neutrino to electron neutrino ratio which did not match that expectation (cf. p. 258 Perkins 2009). This was again a sign for neutrino oscillations and will be discussed in more detail in the next subsection.

Lastly, high-energy neutrinos with energies in the TeV range come from galactic or extragalactic accelerators. The accelerators can be pulsars, supernova remnants, or active galactic nuclei. They are point sources for high-energy gamma rays in the order of TeV. The gamma rays can be produced by synchrotron radiation of high-energy electrons, but also by pion decay: $\pi_0 \longrightarrow 2\,\gamma$. The pion decay not only produces gamma rays but also high-energy neutrinos (cf. p. 264 Perkins 2009). Using neutrino detection in addition to gamma detection allows for improved inferences about the properties of the point source. This relates to the wide field of multi-messenger-methods in particle astrophysics and shows the great importance of understanding the neutrino's properties.

2.1.2 Neutrino Oscillations

Multiple experiments with different neutrino sources indicate a change of the neutrino flavor between source and detector. The Sudbury Neutrino Observatory (SNO), a heavy-water Cherenkov detector (Ahmad et al. 2001), together with Super-Kamiokande (Fukuda et al. 1998) showed that neutrinos change their flavor and thereby solved the solar neutrino problem. This flavor change phenomenon is explained with neutrino oscillations.

Already in the 1960s neutrino oscillations were proposed: Maki, Nakagata and Sakata (1962) developed a theory for neutrino mixing based on two types of neutrinos. This theory was developed further by Pontecorvo (1968).

The idea is that while neutrinos interact via their flavor eigenstates $\nu_\mathrm{e}, \nu_\mu, \nu_\tau$ they propagate through space as mass eigenstates ν_1, ν_2, ν_3. This is similar to the theory of coupled oscillators. For an easier explanation it is now reduced to only two neutrino types. To make the conversion of electron neutrino to muon neutrino possible, the mass eigenstates ν_1 and ν_2 need to be linear combinations of ν_e and ν_μ, a possible realization being

$$\nu_1 = \cos(\theta)\nu_\mu - \sin(\theta)\nu_\mathrm{e}, \nu_2 = \sin(\theta\nu_\mu) + \cos(\theta\nu_\mathrm{e}). \tag{2.1}$$

If the flavor of the neutrino is known at one point in time, the time evolution operator of Schrödinger's equation can be used to determine the probability that a flavor change has occured. For example starting with an electron neutrino, the probability that it has transformed into a muon neutrino is

$$P_{\nu_\mathrm{e} \longrightarrow \nu_\mu} = \left[\sin(2\theta) \cdot \sin\left(\frac{\Delta m_{12}^2 \cdot c^4}{4\hbar E} \cdot t\right)\right]^2 . \tag{2.2}$$

The oscillation depends on the *mixing angle* θ and the quadratic mass differences between the mass eigenstates. This can be applied analogously to the other known neutrino types. One can also form a mixing matrix U, known as the *PMNS matrix*, which can be expressed in terms of the three angles θ_{12}, θ_{23}, θ_{13} and one phase factor δ_CP[2] (cf. pp. 390ff. Griffiths 2008).

The two squared mass differences Δm_{12}^2 and Δm_{23}^2 and the mixing angles θ have been experimentally determined. Recent results are listed in table 2a.

[2] δ_CP denotes the CP violation phase.

Due to the very small mixing angle θ_{13}, the mixing between solar ($ij = 12$) and atmospheric neutrinos ($ij = 23$) is effectively decoupled. Because of this decoupling, it is often precise enough to describe neutrino oscillations with only two-neutrino mixing as has been done in equation (2.1) and equation (2.2).

The phase factor δ_{CP} is difficult to determine because it contributes to the PMNS matrix multiplied with the very small $\sin(\theta_{13})$. Efforts to determine it are already being made, for example with the T2K experiment (Evslin et al. 2016).

Measurements investigating the neutrino oscillation only provide information about the squared mass differences of the neutrinos. Values for the absolute mass are still to be determined and methods for that will be discussed in the next section.

2.2 Neutrino Mass Measurement

There are several different approaches to measuring neutrino mass. One is the indirect determination via cosmological parameters that depend on the neutrino mass value. An example are measurements of the cosmic microwave background (Ade, P. A. R. et al. 2014). They provide a model-dependent upper limit for the sum of neutrino mass eigenstates: $\sum_i m_i < 0.23\,\mathrm{eV}$.

Another model-dependent approach is the measurement via the neutrinoless double beta decay. The *ordinary* double beta decay, proposed by Maria Goeppert-Mayer (Goeppert-Mayer 1935) and first observed in 1987 (Elliott et al. 1987), describes the decay

$$^{\mathrm{A}}_{\mathrm{Z}}\mathrm{X} \longrightarrow {}^{\mathrm{A}}_{\mathrm{Z+2}}\mathrm{X} + \mathrm{e}^-_1 + \mathrm{e}^-_2 + \bar{\nu}_{\mathrm{e},1} + \bar{\nu}_{\mathrm{e},2}\,.$$

This decay is only possible for nuclei for which the normal beta decay is energetically excluded. Ettore Majorana (1937) proposed the *neutrinoless* double beta decay, which can be possible if neutrinos are their own antiparticles – now known as Majorana particles.

There are multiple experiments searching for this decay, one of them being the GERDA

Table 2a: **Neutrino mixing values.** The values listed here were obtained from Patrignani et al. (2016). They were calculated with the assumption of normal mass hierarchy ($m_1 < m_2 < m_3$).

ij	$\sin^2(\theta_{ij})$	Δm^2_{ij} in eV^2	sources
12	0.304(14)	$7.53(18) \cdot 10^{-5}$	solar, reactor
23	0.51(5)	$2.44(6) \cdot 10^{-3}$	atmospheric, accelerator
13	0.0219(12)		reactor, accelerator

experiment at the Gran Sasso Laboratory (Agostini et al. 2013). Up until today only lower limits for the half-life of neutrinoless beta decay have been found. The Majorana neutrino mass from these experiments is the coherent sum $m_{\beta\beta} = |\sum_i U_{\mathrm{e}i}^2 \cdot m_i|$.

Yet another approach is the model-independent method via the kinematics of beta decay. Here the electron neutrino mass $m_{\nu_\mathrm{e}} = \sqrt{\sum_i |U_{\mathrm{e}i}|^2 \cdot m_i^2}$ is measured. This method will now be explained in detail.

As described above, a beta decay creates an electron and an electron antineutrino. The transition energy of the decay is split up between electron and electron antineutrino. This produces the characteristic continuous electron energy spectrum as shown in figure 2b.

The Fermi theory of beta decay describes this process, treating it as a transition dependent on the interaction strength between the initial and final states. The transition probability between the initial i and final state f can be described with Fermi's Golden rule. Therefore the transition rate for the electrons is given by

$$\frac{d^2N}{dt\, dE_f} = \frac{2\pi}{\hbar}|M_{if}|^2 \rho(E_f).$$

M_{if} is the transition matrix element, ρ_f the density of final states. In a simplified form the transition rate for a bare and infinitely heavy nucleon can be written as

$$\frac{d^2N}{dt\, dE_f} \approx F(E,Z+1)\cdot p(E+m_\mathrm{e})\cdot(E_0-E)\cdot\sqrt{(E_0-E)^2-m^2(\nu_\mathrm{e})}\cdot\theta(E_0-E-m^2(\nu_\mathrm{e})). \quad (2.3)$$

The Fermi-Function $F(E,Z+1)$ describes the electromagnetic interaction between the electron and the daughter nucleus (cf. pp. 29ff. Altarelli 2003). In this simplified version, one important point is already apparent: the spectrum depends on the electron neutrino mass value.

As shown in figure 2b, the electron neutrino mass value becomes manifest in the endpoint of the spectrum. Here the electron carries away most of the energy as kinetic energy, leaving the neutrino with a kinetic energy close to zero.

In order to determine the neutrino mass based on this effect, a beta source with high intensity, moderate endpoint energy and preferably a simple molecular structure is required. The isotope $^{187}_{85}\mathrm{Rh}$ used by the experiment MARE (Andreotti et al. 2007) is one suitable candidate. For MARE, micro-calorimeter arrays with dielectric $\mathrm{AgReO_4}$ were used to measure the complete beta spectrum.

Another example is the ECHo experiment (Gastaldo et al. 2014), where the isotope $^{163}_{67}\mathrm{Ho}$ was used and the energy spectrum E_c of an electron capture was measured:

$$^{163}_{67}\mathrm{Ho} + \mathrm{e}^+ \longrightarrow {}^{163}_{66}\mathrm{Dy}^* + \nu_\mathrm{e}\,, \quad {}^{163}_{66}\mathrm{Dy}^* \longrightarrow {}^{163}_{66}\mathrm{Dy} + E_c\,.$$

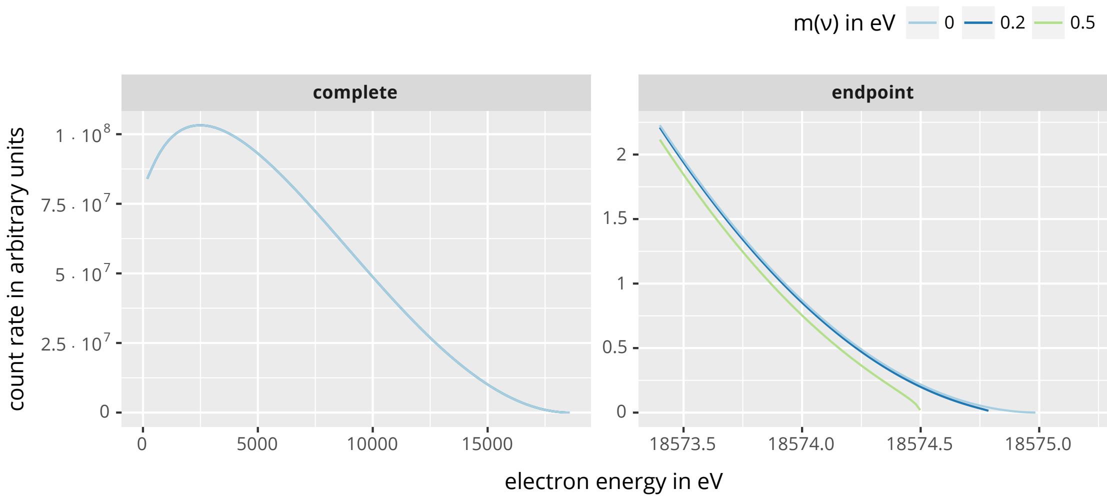

Figure 2b: **Energy spectrum of beta decay electrons.** This schematic energy spectrum for beta decay electrons of tritium shows the influence of the neutrino mass on the endpoint E_0 region. Here the endpoint was defined as $E_0 = 18.575\,\mathrm{keV}$. Figure inspired by (Angrik et al. 2005).

The energy spectrum measured with magnetic calorimeters is sensitive to the electron antineutrino mass.

The isotope tritium ^{3}H, having a low endpoint energy $E_0 = 18.6\,\mathrm{keV}$, a short half-life of 12.3 a and a simple molecular structure is a suitable beta emitter for measuring the neutrino mass. The tritium decays to ^{3}He while emitting an electron and an electron antineutrino: $^3\mathrm{H} \longrightarrow {}^3\mathrm{He} + \mathrm{e}^- + \bar{\nu}_\mathrm{e}$ (cf. p. 34 Angrik et al. 2005).

Experiments in Troitsk (Aseev et al. 2011) and Mainz (Kraus et al. 2005) measured the endpoint region of the tritium beta decay electron spectrum using a *magnetic adiabatic collimation combined with an electrostatic filter*, or MAC-E filter. The Mainz experiment derived an upper limit for the electron neutrino mass of $m(\nu_\mathrm{e}) \leq 2.3\,\mathrm{eV/c^2}$ and the Troitsk experiment one of $m(\nu_\mathrm{e}) \leq 2.05\,\mathrm{eV/c^2}$.

The KATRIN experiment incorporates methods developed at Mainz and Troitsk, but is designed to improve on the experimental sensitivity by about a factor of 100. The next chapter explains the means by which that improvement is made possible and details the setup of the experiment.

3 KATRIN Experiment

In this chapter the general setup of the KATRIN experiment will be presented. The first section describes the general measurement principle using a MAC-E filter to measure an integrated electron spectrum. Afterwards starting with the Tritium source and following the path of the beta electrons up to the detector the whole KATRIN beamline will be introduced.

The chapter concludes with a short section presenting the commissioning measurements with conversion electrons of ^{83m}Kr performed in July.

Any details found in this chapter regarding the setup of the KATRIN experiment are based on the design report (Angrik et al. 2005) unless a different source is mentioned.

3.1 Measurement Principle

An electron entering a homogeneous magnetic field angular to the field-lines is forced on a cyclotron motion along the field-lines due to the Lorentz force. Therefore the magnetic field is acting as guide field for the electrons.

Adding an electric field produces a retarding potential that only electrons with energies above a threshold, defined by the electric field, can pass. A combination of magnetic guide field and electric field is called MAC-E filter. It improves the ordinary pure magnetic spectrometer, where only electrons with a certain momentum reach the detector.

The MAC-E filter type spectrometer has been proposed by Beamson, Porter and Turner (1980). The idea was adapted for the search for electron neutrino masses (Lobashev 1985; Picard 1992). In figure 3a, where the MAC-E filter setup of the KATRIN main spectrometer (see section 3.2) is shown, one can see the properties of a MAC-E filter.

Electrons entering the spectrometer are guided by an axially symmetric inhomogeneous magnetic field created by two superconducting solenoid magnets on both ends of the spectrometer. Inside the spectrometer the magnetic field decreases due to the widening of the magnetic field lines, as shown in figure 3a. The kinetic energy of the electrons can be described as superposition of parallel $E_{\parallel}$ and anti-parallel $E_{\perp}$ to the magnetic field lines. The Lorentz force of a magnetic field always acts perpendicular to the electrons motion, this way

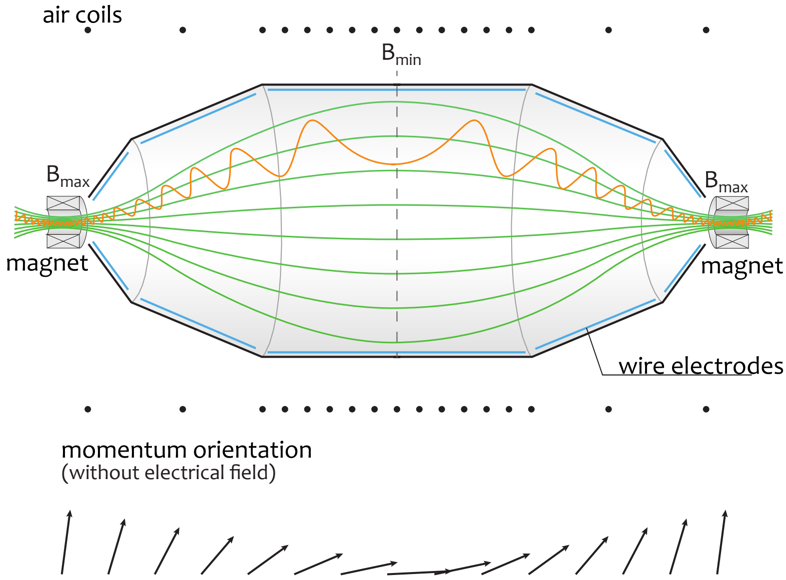

Figure 3a: **Principle of the MAC-E filter.** This figure is adapted from (p. 29 Schimpf 2017). The green lines represent the magnetic field lines created by the superconducting magnets on each side of the spectrometer tank. Air coils around the spectrometer provide the possibility to fine tune the magnetic field inside the spectrometer. The orange line indicates the cyclotron motion of the electrons around the magnetic field lines. The arrows below show the transformation of the electrons momentum due to the magnetic field gradient.

the electrons magnetic momentum can be described as:

$$\mu = \frac{E_\perp}{B}. \tag{3.1}$$

The electrons can be described in non-relativistic terms due to their low kinetic energy ($\sim$18 keV).

It can be shown (cf. Beamson et al. 1980) that the magnetic momentum is invariant. This means a decrease in the magnetic field strength B causes a decrease of the electron's kinetic energy perpendicular to the magnetic field $E_\perp$, only then equation (3.1) stays constant. For $E_\perp$ to decrease $E_\parallel$ needs to increase.

The electrons flying almost parallel to the magnetic field-lines inside the spectrometer due to the decreasing magnetic field. The spectrometer vessel is set on high voltage, creating an electrostatic barrier for the electrons, called retarding potential U_{ret}. All electrons fulfilling the transmission condition:

$$E_\parallel > e \cdot U_{\text{ret}}$$

are accelerated again after passing the analyzing plane (marked with a dashed line in figure 3a) and reach the detector.

Setting the retarding potential to different voltages enables the scanning of the integrated electron spectrum with the MAC-E filter. This already implies the requirements on the high voltage system: The voltage needs to operate at different setpoints around the tritium endpoint of 18.6 keV and needs to be stable on a 3 ppm level. Chapter 7.1 presents the influence of high voltage instabilities on the neutrino mass measurements and deduces the stability requirements. How the stability requirements are met will be shown in chapter 4.

The invariance of the magnetic momentum indicates the possible energy resolution that can be achieved with a MAC-E filter depends on the ratio between the maximal and the minimal magnetic field strength:

$$\frac{\Delta E}{E} = \frac{B_{\text{min}}}{B_{\text{max}}}.$$

In KATRIN the MAC-E filter is operated at a nominal filter width of 0.93 eV using the design values $B_{\text{min}} = 3 \cdot 10^{-4}$ T and $B_{\text{max}} = 6$ T at $E = 18.6$ keV.

If the tritium source would be placed directly in the B_{max}-field one would have an acceptence angle of 2π for the electrons. This has the disadvantage that electrons that already scattered inside the source are also accepted. To avoid that the source is placed in a magnetic field of B_s. This way one again creates a magnetic bottle, which is used to only accept electrons with a starting angle below:

$$\sin\theta_{\text{max}} = \sqrt{\frac{B_s}{B_{\text{max}}}} = 50.77°.$$

Here the design value for the magnetic field at the source $B_s = 3.6$ T is used.

With this one can define an analytic transmission function for electrons in the MAC-E filter, see figure 3b. One can see that electrons with energies smaller than $e \cdot U_{\text{ret}}$ have a transmission probability of zero and of one for electron energies greater than $e \cdot U_{\text{ret}} + \Delta E$. Inbetween the transmission probability increases with increasing energy.

The KATRIN experiment is equipped with three MAC-E filters. The first MAC-E filter, the *pre-spectrometer*, is used to prefilter electrons. In its standard operation mode it will filter electrons with energies smaller than 18.3 keV. Electrons that transmit through the pre-spectrometer are guided into the *main spectrometer*. The main spectrometer is again a MAC-E filter and is used in standard operation mode to scan energies around the tritium endpoint.

The third spectrometer is called *monitor spectrometer* and is the spectrometer taken from the Mainz neutrino mass experiment. Instead of tritium decay electrons it measures conversion electrons from $^{83\text{m}}$Kr and provides a high voltage monitoring against a nuclear standard. All three spectrometers will be explained further in the next section.

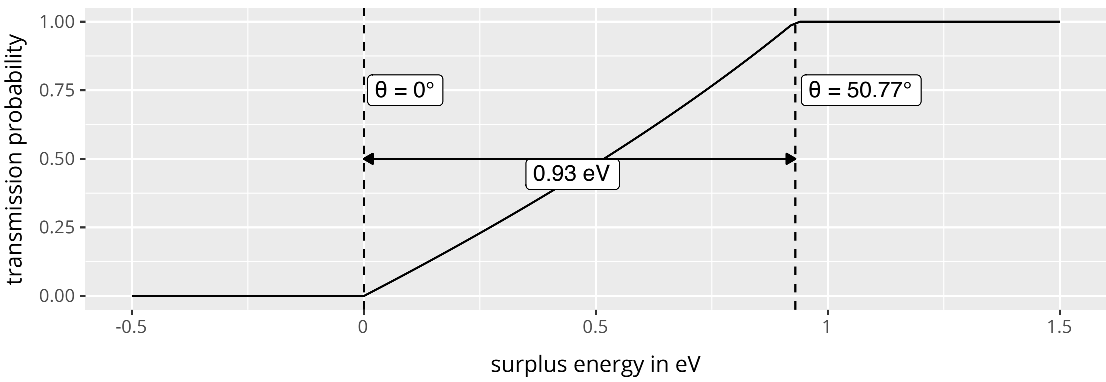

Figure 3b: **Transmission function of a MAC-E filter.** This shows the transmission probability for an electron entering the KATRIN main spectrometer with a surplus energy in relation to eU_0, where U_0 is the retarding potential

3.2 Experimental Setup

This section will explain the experimental setup of KATRIN along the beamline, see figure 3c following the electrons emitted from the tritium source up to the detector. The beamline can be divided in four main sections: source, transport, spectrometer and detector section.

3.2.1 Tritium Source

Source for the measured beta electrons is a windowless gaseous tritium source (WGTS)[1]. The WGTS beam tube is a 10 m long and 90 mm diameter open cylinder inside a homogeneous magnetic field of 3.6 T. The tritium gas will be injected in the center of the beam tube and pumped at both ends with constant pumping speed. The beam tube is cooled down to 30 K.

The tritium source activity scales linearly with the tritium purity multiplied with the column density. The column density is the number of molecules in the fluxtube volume with the design value of $5 \cdot 10^{17}$ molecules/cm^2. The energy losses of electrons due to inelastic scattering inside the source depend on the column density and therefore have an influence on the measured neutrino mass value. To monitor the column density experimental parameters, such as beam tube temperature, injection and outlet pressure are monitored.

Impurities in the tritium gas lead to different recoil energies and therefore as well influence the neutrino mass value. The aimed purity is ≥ 0.95, with a small mixture ≤ 0.1 of deuterium. To monitor the purity a *laser Raman spectroscopy system* (LARA) has been developed. LARA is placed inside the Inner Loop System, which stabilizes the tritium injection rate and filters non-hydrogen molecules (Priester et al. 2015).

[1]Additional reference for this section about the WGTS is Babutzka et al. (2012).

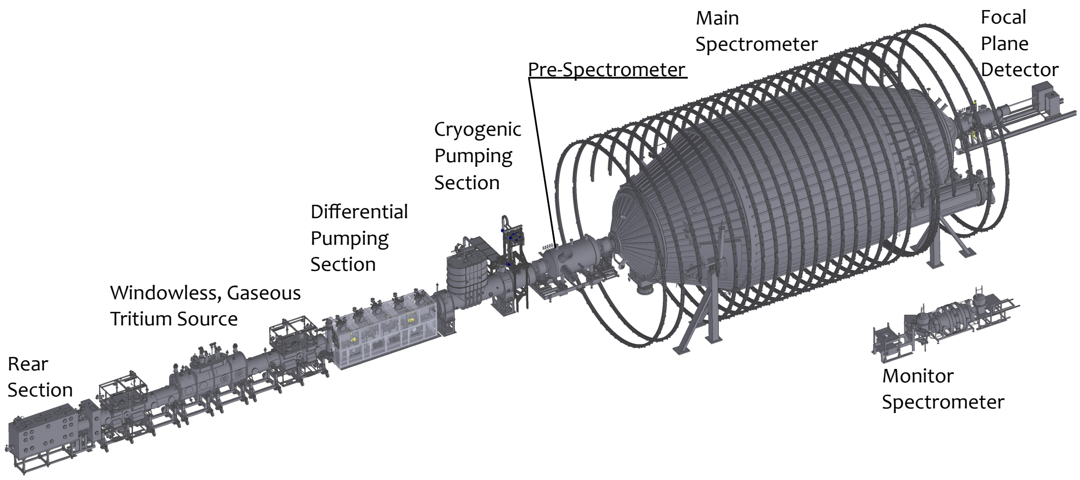

Figure 3c: **KATRIN Beamline.** This figure shows the general setup of the KATRIN beamline. In sections 3.2 and 3.3 descriptions to the labeled components can be found. The picture is adapted from Arenz et al. (2018a).

In the calibration and monitoring section (CMS) two systems monitoring the source activity are located. Both of them monitor beta electrons interacting with the rear wall. One uses the Faraday cup principle and measures currents induced by the beta electrons. The other one uses beta-induced x-ray spectroscopy (BIXS), to detect x-rays produced by the beta electrons.

Additionally, an electron gun (currently under construction) inside the CMS can be used to determine the column density. The electron gun produces via the photo-electric effect monoenergetic electrons, with known intensity, known exit angle and adjustable kinetic energy. Measuring the electrons with the KATRIN spectrometer section gives information about energy losses of the electrons on their way through the beamline and permits to deduce the column density in the WGTS. This measurement can not be done simultaneously to the neutrino mass measurements, therefore it will be used periodically as cross-calibration check for the column density.

Summing up, the WGTS supplies the KATRIN beamline with beta electron out of tritium decay, together with the monitoring possibility of energy losses of the electrons.

3.2.2 Transport System

To ensure that only electrons reach the spectrometer, tritium exiting the WGTS needs to be filtered. This is done in two stages: First with a differential pumping section (DPS) and second with a cryogenic pumping section (CPS).

The first part of the DPS, located on both sides of the WGTS (forwards: DPS1-F and rearwards: DPS1-R) continuously pumps tritium. The second part DPS2-F is located inside the transport section behind the WGTS. Here five beam tube segments are inclined by 20° to each other and inbetween the segments are four pumping ports (Lukić et al. 2012). Magnetic fields guide the electrons through the tilted beam tube.

Neutral atoms and molecules not pumped out by the DPS1-F part are held back by the tilted beam tube in the DPS2-F. Given that they are not magnetically guided they collide with the beam tube walls and can be pumped out by the turbo molecular pumps. For the removal of positive charged ions dipole electrodes are installed inside the DPS. Their electric field deflects the ions on to the beam tube surface where they can be neutralized and pumped out (Kosmider 2012).

The CPS[2] is designed as a *cryosorption* pump, that adsorbs incoming gas on an argon frost layer. Its beam tube elements are again tilted to each other, utilizing the same effect as the DPS. During neutrino measurements the CPS is run at a temperature of 3 K. Design values predict that after 60 d of measurement the argon frost layer has accumulated an activity of 1 Ci. At this point the CPS beam tube part needs to be heated up to 100 K to defrost and purge the tritium with injected warm helium gas. The tritium-argon-helium mixture will then be pumped back to the tritium purification infrastructure and afterwards a new argon frost layer can be applied.

In conclusion, the transport system guides electrons from the WGTS to the spectrometer section, while their energy stays unchanged at the meV level. At the same time the WGTS provides a tritium flow reduction by more than fourteen orders of magnitude. The resulting tritium contamination will be therefore not only well below safety guidelines but also prevent additional background due to tritium in the spectrometers.

3.2.3 Spectrometer System

To analyze the beta decay electrons two spectrometers of MAC-E filter type as described above, are installed in tandem configuration. The first spectrometer is the pre-spectrometer, a cylindrical 3.38 m long stainless steel tank with an outer diameter of 1.7 m. Its dimensions are comparable with the predecessor MAC-E filters set up in Mainz and Troitsk.

The purpose of the pre-spectrometer is to reduce the beta electron flux from 10^{10}/s to 10^4/s as it filters electrons with kinetic energies less than 18.4 keV. For the neutrino mass measurements only electrons in the endpoint region of 18.6 keV are of relevance. This means the filtering electrons with kinetic energies less than 18.4 keV, does not influence the measurements.

[2](Kosmider 2015) is used as additional reference for the description of the CPS.

Beta electrons in the main spectrometer can induce additional background due to ionization of resdiual gas molecules. The flux reduction by the pre-spectrometer decreases the chances for these additional background processes. An energy resolution of about 100 eV is sufficient enough for the flux reduction.

Both spectrometers need to be operated at ultra high vacuum conditions with pressures below 10^{-11} m bar to reduce possible background processes. To achieve these conditions a combination of turbo molecular (TMP) and non-evaporable getter (NEG) pumps is used.

The main spectrometer is like the pre-spectrometer a stainless steel tank but with a total length of 23.28 m and at the cylindrical section a diameter of 9.8 m. This produces a volume of $1240\,m^3$ and an inner surface of $690\,m^2$ that needs to be pumped to achieve the vacuum requirements. Three pump ports are installed and each equipped with a custom made NEG pump. The three outer pump ports are additionally equipped with three TMP, with an effective pumping capacity of $10^3\,m^3/s$ for hydrogen (cf. Arenz et al. 2016).

Investigations showed that the NEG pumps emanate Radon (^{219}Rn) whose alpha decay produces background in the spectrometer before it is pumped by the TMPs. To prevent the Radon from entering the flux tube of the spectrometer LN2 cooled copper baffles are installed (Fränkle et al. 2011).

For the MAC-E filter principle to work, a magnetic field and an electrostatic potential are needed. The magnetic field for the main spectrometer is produced by two superconducting magnets on both sides of the spectrometer. The magnet located on the side connected to the pre-spectrometer creates the magnetic guiding field together with the magnet on the detector side. A magnetic air coil system consisting of two parts: the low field correction system (LFCS) and the earth magnetic field compensation system (EMCS), allows for precision adjustments of the magnetic field shape inside the spectrometer.

The main and the pre-spectrometer can be set on a high voltage (up to 35 kV) creating a retarding potential for the beta electrons. Both spectrometers have additionally an inner electrode system providing a fine tuninng of the electrical field and screening background electrons from the wall. The precision setup, stability and monitoring of the high voltage system is vital for the MAC-E filter to work. The details of the high voltage setup will be explained in the succeeding section.

3.2.4 Detector System

Filtering electrons with the introduced high energy resolution integrating high-pass filter on its own does not generate an electron spectrum. For this the electrons passing through the main spectrometer need to be counted.

Electrons exiting the spectrometer are magnetically guided into the focal-plane detector system (FPD)[3]. There a post-acceleration electrode increases their energy and they strike a 148-pixel detector. The detector is made of a p-i-n-diode array on a single silicon wafer. The 148 segments of equal size are arranged circular in a dart board design and can be grouped into twelve rings each with twelve pixels. The detector's bulls eye consists of four pixels. This pixel distribution allows a spacial resolution making the measurement of inhomogenities in the electric and magnetic field possible.

The FPD system includes a shielding and a veto system for background reduction. For energy calibrations an electron source and a gamma emitter is included inside the FPD.

3.2.5 Monitor Spectrometer

The monitor spectrometer is the third spectrometer of KATRIN using the MAC-E filter principle. It is the repurposed spectrometer from the Mainz neutrino mass measurements. Instead of measuring beta decay electrons from tritium it is rebuilt to measure conversion electrons emitted by an implanted ^{83}Rb/$^{83\mathrm{m}}$Kr source.

Choosing implanted ^{83}Rb/$^{83\mathrm{m}}$Kr as calibration and monitoring source for the KATRIN energy scale stability has several reasons (cp. Zbořil et al. 2013). First the measured electrons should exhibit a well defined discrete spectrum. This is fulfilled by the $^{83\mathrm{m}}$Kr conversion electron lines. The K-32 line has an energy of 17.8 keV and a natural width of 2.8 eV (full width at half maxium)(Picard et al. 1992). This energy makes $^{83\mathrm{m}}$Kr predestined for the KATRIN energy scale due to its close proximity to the tritium endpoint energy.

Another criteria for the calibration source is that its half-life should be long enough to last during a normal KATRIN neutrino mass measurement run.[4] Therefore a ^{83}Rb implanted substrate is used as generator for krypton. It has a half-life of $T_{1/2} = 86.2(1)$ d (McCutchan 2015). ^{83}Rb generates $^{83\mathrm{m}}$Kr via electron capture, which itself only has the relatively short half-life of 1.83 h (McCutchan 2015).

Sharing the potential with the main spectrometer and continuously measuring during neutrino measurements the monitor spectrometer provides an independent monitoring of the energy scale stability in KATRIN. This is done by measuring line positions of $^{83\mathrm{m}}$Kr. Monitoring changes of the measured line positions can be used to deduce instabilities in the high voltage at the main spectrometer (Erhard et al. 2014).

[3]Details of the FPD system are taken from (Amsbaugh et al. 2015).

[4]Due to the necessity to refresh the argon frost layer in the CPS, neutrino mass measurement will be halted every two months (cf. section 3.2.2).

3.3 Commissioning Measurements with Conversion Electrons of ^{83m}Kr

The previous section already introduced the usefulness of ^{83m}Kr for energy scale stability investigations. In the commissioning measurement phase in July 2017 two additional ^{83m}Kr sources were utilized. Details on this measurement phase were taken from (Arenz et al. 2018a).

One source was ^{83m}Kr in gaseous form, injected in the WGTS. The WGTS was operated at a temperature of 100 K instead of the 30 K for neutrino measurements (cf. section 3.2.1) to ensure an optimized gaseous ^{83m}Kr flow. This gave the opportunity to investigate electrons emitted by an isotropic source inside the WGTS, guided through the whole KATRIN beamline, filtered with the main spectrometer and counted at the detector. Injection of gaseous ^{83m}Kr in the WGTS and measuring the conversion electron lines can also be used to determine the distribution and central value of the electric potential inside the WGTS.

The second source was ^{83m}Kr in condensed form placed inside the CPS. Here ^{83m}Kr is condensed on a highly oriented pyrolytic graphite substrate (HOPG, also used at the monitor spectrometer for the implanted sources), that is cooled down to 26 K. Beneficial of this source is the isotropic electron emission, high count rates and simple maintenance. In contrast to the gaseous source the condensed source illuminates not the complete detector, but a small region with high intensity.

^{83m}Kr has a variety of conversion electron lines. The one in the region of the tritium endpoint, the K-32 line was already described in the previous section. Another one, measured during this measurement phase is the L_3-32 line. It is again the 32 keV gamma transition but starting from the L-subshell instead of the K-subshell. Subtracting the binding energy (Dragoun et al. 2004) for the K-subshell the kinetic energy of the conversion electron is at 30.5 keV.

Additionally conversion electrons lines from the 9.4 keV gamma transition were measured. For these measurements the main spectrometer needed to be operated at three different voltage ranges: 9 kV, 17 kV and 30 kV. In these voltage ranges voltage scans around the line positions were performed to measure the integrated line spectra.

In addition to the described features the commissioning measurement in July provided an excellent trial of the high voltage setup: especially testing the switching between different voltage setpoints and more generally testing the monitoring of the high voltage. The succeeding chapters will first introduce the high voltage setup in general and then outline high voltage anomalies discovered during this commissioning measurement.

4 High Voltage Setup of the KATRIN Experiment

4.1 High Voltage Generation and Distribution

All three spectrometers – pre-spectrometer, main spectrometer and monitor spectrometer – are MAC-E filters and therefore need to have a retarding potential for the electrons (cf. chapter 3).

To create the retarding potential, the spectrometers are equipped with high voltage sources directly connected to the spectrometer vessel. An exception being the monitor spectrometer where the vessel is insulated. Additionally an inner electrode system is installed inside the vessels. This not only allows for fine tuning of the retarding potential but also offers the possibility of background reduction.

This chapter begins with a brief introduction to the control of the high voltage system. Following are details for the high voltage implementation at the three spectrometers.

4.1.1 Safety Precautions and Control of the High Voltage System

Setting a large stainless steel tank like the pre-spectrometer, or like the even larger main spectrometer on a potential of up to 35 kV is not a simple task. Therefore many security precautions are in place. For example, the whole area is restricted and separated with a high fence. High voltage both at the main and pre-spectrometer is only possible after going through a strict safety plan.

A grounding switch ensures the immediate grounding of the whole system as soon as one door to the restricted area is opened. These precautions are of importance not only to ensure personnel safety, but also to ensure the safety of all the delicate electronics inside and around the spectrometers. More details on the safety precautions can be found in (Kraus 2016).

As soon as there is clearance for high voltage use, the spectrometers can be set on high voltage. The power supplies used at pre- and main spectrometer can be controlled remotely and their sensor values are stored in the Advanced Data Extraction Interface (ADEI)[1]. ADEI provides access to slow control data via a web service interface (Chilingaryan et al. 2010).

[1]The Advanced Data Extraction Interface (ADEI) for sensor data at KATRIN is accesible at http://katrin.kit.edu/adei-katrin/. This offers the possibility of a near real-time monitoring of sensors at KATRIN.

The sensor values for power supplies, stored in ADEI are divided into two groups: control values sent to the device, and read back values received from the device. An overview for the sensor values is given in table 4a.

Every high voltage power supply is connected to a CompactRIO system,[2] combining real-time controllers with **R**econfigurable **I**nput/**O**utput modules. A dedicated control computer terminal for expert access, called the "Experten-PC", is used to communicate with the CompactRIO.

To send control values to the power supplies one can use a LabVIEW[3] program on the Experten-PC. To control the voltages more remotely for example via the Focal Plane Detector control program, the central data acquisition and control system, called ZEUS can be used (Lefhalm, Krieger 2005). This method was used during the commissioning measurement phase with krypton. One disadvantage are the communication times in the order of multiple seconds. To circumvent this, a faster method has recently been implemented. Here the run control directly communicates with the high voltage control without a detour over ZEUS. It is planned to fine-tune and test this new method further, to ensure an immediate voltage control during neutrino mass measurements.

Table 4a: **Typical sensor values for a voltage power supply.** Mapping between the sensor value identification in ADEI and its meaning for the power supply. Sensor values can be assigned to two different kinds: values sent to the device *control* values, called "SOLL" in ADEI, and values received from the device *read back*, called "IST" in ADEI.

identification	meaning	group
U_SOLL	voltage setpoint	control, read back
U_IST	actual voltage value	read back
Rampe	maximum allowed ramping speed	control, read back
I_MAX	maximum allowed current	control, read back
I_IST	actual current value	read back
I_Begrenzt	boolean value for current limiting	read back
Warnung	boolean value for warning message	read back
Fehler	boolean value for error message	read back

[2] More information to the CompactRIO from National Instruments can be found on http://www.ni.com/compactrio/

[3] LabVIEW: "Laboratory Virtual Instrumentation Engineering Workbench" provides a visual programming language for data acquisition and processing (https://www.ni.com/labview).

4.1.2 High Voltage at Pre-Spectrometer

As described in section 3.2.3 the pre-spectrometer is used as pre-filter for the beta-electrons. Here the requirements for the energy resolution are less stringent than at the main spectrometer.

The inner electrode system consists of a single-layer wire electrode in the center of the spectrometer and a full metal cone electrode at both ends of the tank.

To ensure the wire electrode does not produce any additional electron background, the electric field close to the wires needs to be small to prevent field emission. This is achieved in using wires with a diameter of 0.5 mm. The wire electrode is installed in a distance of 5 cm from the vessel wall and between each wire is a space of 2 cm.

The west and east half[4] of the inner electrodes can be individually set on a high voltage. This provides the possibility of *dipole mode* operation. The dipole mode creates an additional electrical field perpendicular to the magnetic field. This induces a $\vec{E} \times \vec{B}$ drift on the electrons in the spectrometer, that can force trapped electrons out of the spectrometer.

Two power supplies, each with two channels, provide the possibility of setting the four electrodes, both cone and wire electrodes, to four different voltages. Given that it is not important for neutrino mass measurement analysis to know the exact voltage values at the pre-spectrometer, the monitoring is reduced to monitor voltage values as measured by the power supplies.

4.1.3 High Voltage at Main Spectrometer

The inner electrode system of the main spectrometer was developed with the experiences gained at the pre-spectrometer. It is developed to ensure fine tuning of the electrical fields inside the spectrometer, to reduce background and to prohibit the formation of penning traps.

It consists of two types of electrodes: wire electrodes and two metal sheet electrodes. The metal sheet electrodes are located on both outer ends of the spectrometer. The wire electrodes are of two types: 28 single-layer modules and 220 double-layer modules. The wire modules are grouped into 15 rings. The rings are again grouped into steep cones, flat cones and the cylindric central part. Additionally they are divided into east and west half. The steep cones consist of single-layered wires, whereas the flat cones and the central part consist of double-layered modules (Prall 2011).

In order to use this complex inner electrode system to its full capacity six power supplies with each 8 channels can set the inner electrodes on positive offset voltages from 0 V to

[4] As orientation: the electrons travel from south to north through the spectrometer.

500 V (Rest 2014). At this point it is important to mention that during the bake-out of the spectrometer[5] some of the double-layer modules were short circuited (Kraus 2016). Therefore setting the layers on different potentials, to achieve an additional background reduction is not possible. Additionally a short circuit exists between ring five and six.

Nevertheless the present configuration still provides a great flexibility in setting the inner electrodes: every ring (except rings five and six), can be set on a different potential, including the possibility to setting the east and west sides to different potentials, with an additional dipole power supply. These inner electrode potentials are positive offsets in respect to the vessel voltage, and are therefore called *offset-potentials*.

The metal sheet electrodes can also be set on a separate potential. During normal operation they will be on the same potential as the vessel potential (Prall 2011). In addition to the offset potential all wire electrodes can be set on a common potential, negative in respect to the vessel voltage. This negative potential of the wires, called *inner electrode common* (IE common), ensures the background reduction via the wire electrodes.

To set the main spectrometer vessel on high voltage, two different power supplies are available: the *precision power supply* of type: FuG HCP 70M-35000 (FuG 2008a) and the main spectrometer *standard power supply* FuG HCN 140M-35000 (FuG 2008b). Both power supplies have built-in customizations. The precision power supply characterizes an especially high stability for voltages, specified as 2 ppm/8h.

In the beginning of the commissioning measurements with ^{83m}Kr the standard power supply was used for test purposes to protect the precision power supply. Afterwards the precision power supply was used during the complete measurement phase. In chapter 6 anomalies of this power supply that occurred during the long-term operation are presented.

4.1.4 High Voltage Stabilization

In order to conduct energy spectroscopy of electrons with a MAC-E filter a stable and reproducible voltage is needed for the retarding potential. Additionally the high voltage creating the retarding potential needs to be monitored.

The first step towards stable voltages is using high voltage power supplies with high intrinsic stability. Nevertheless two things remain: First, every power supply has an inert drift of the voltages, this needs to be monitored closely. This will be discussed in the succeeding section. Second: A fluctuation free voltage is needed. The power supplies are able to produce a quite constant voltage, but there are always remaining AC components in the voltage.

One example for an AC component is the mains frequency coupling into the voltage. This

[5]The bake-out is perfomed to increase the vacuum conditions inside the spectrometer vessel. During the bake-out the complete spectrometer is heated up to temperatures of 350 °C.

creates a voltage ripple with a frequency of about 50 Hz. Due to its dimensions and consisting mainly of conducting materials the main spectrometer is prone to act as an antenna for propagating electromagnetic waves. The coupling of the electromagnetic waves into the high voltage leads to instabilities (Kraus 2016).

To actively counteract AC noise in the high voltage at the main spectrometer a *post regulation system* is in place. Figure 4b shows the high voltage generation, monitoring and its stabilization with the post regulation system for the retarding potential in the main spectrometer.

The post regulation can be divided into three main parts. The first part measures the AC component of the high voltage at the main spectrometer with a decoupling capacitor, also called *ripple probe*. The signal is amplified with a buffer amplifier and connected to a precision voltage regulator.

The voltage regulator, the second part of the post regulation, receives a voltage setpoint converted with a 20 bit digital-analog-converter. The setpoint deviation is determined in two simultaneous steps. One is measuring the spectrometer voltage with an auxiliary high voltage divider. In the other step the signal of the ripple probe is picked up.

The third part, the vacuum triode shunt regulator actively counteracts voltage deviations measured by the ripple probe. A triode consists of three main elements: anode, cathode and a control grid. Via a voltage at the control grid the current between the anode and cathode is regulated. At the post regulation system the control grid is controlled via fiber-optics by the voltage regulator. This shunt regulator setup provides a high control rate and is able to smooth out voltage instabilities with frequencies up to 1 MHz. Therefore the post regulation is able to suppress the 50 Hz power-grid interference. 21 nF capacities (see 4b) are installed to suppress frequencies above 1 MHz.

Measurements demonstrating the successful operation of the post regulation system are shown in section 4.2.1. During these measurements the ripple probe was used as an additional monitoring device for the voltage stability.

4.2 Monitoring of Main Spectrometer Vessel Potential

The previous section presented the successful efforts made to equip the main spectrometer with a stable retarding potential. In order to perform meaningful analysis of measurements with the main spectrometer a voltage monitoring is needed. On the one hand measuring voltage values is indispensable for the interpretation of electron rates measured at the detector. This is needed during neutrino mass measurements with beta spectrum electrons, as well as with commissioning measurements with ^{83m}Kr conversion electrons, and other measurements where electron spectra are measured with the main spectrometer.

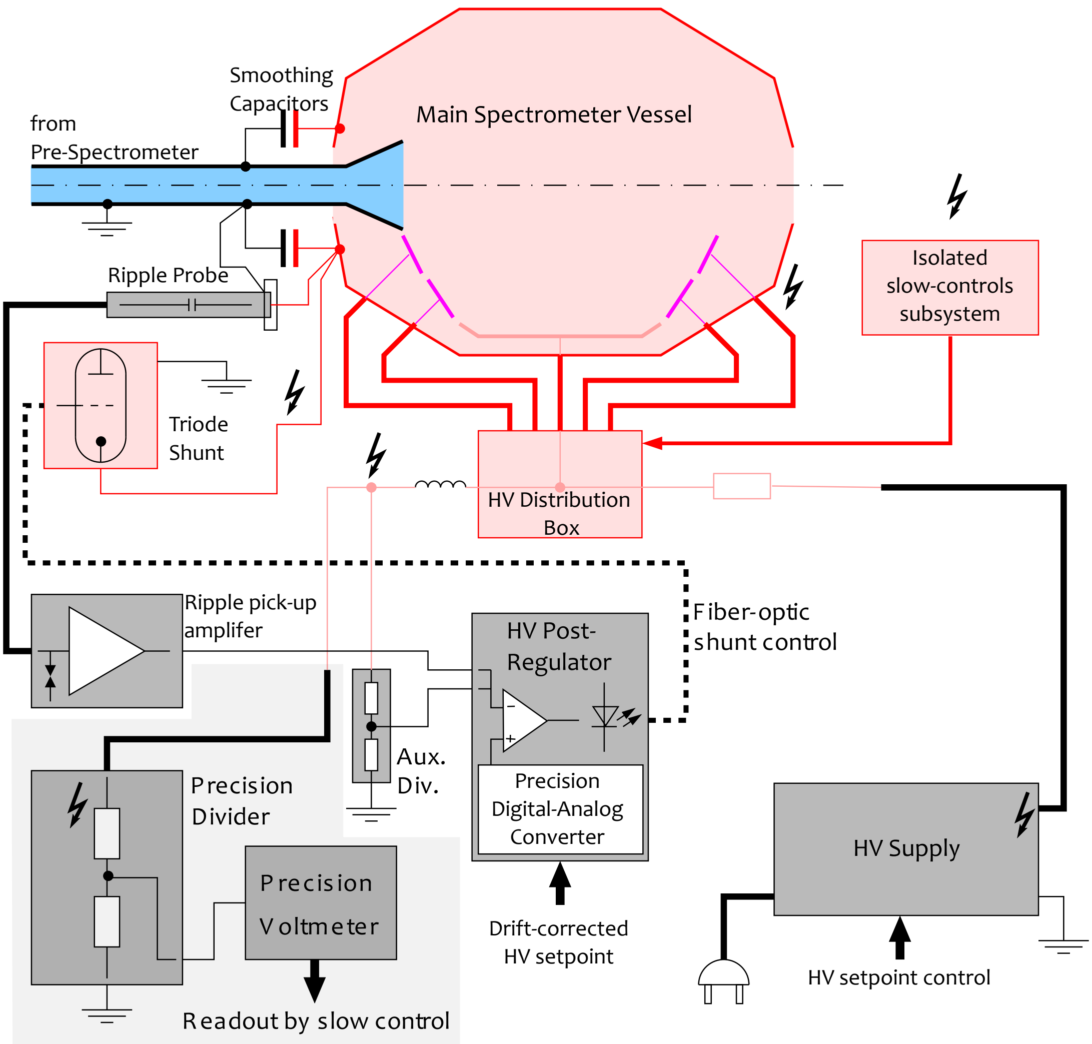

Figure 4b: **High voltage generation, stabilization and monitoring at the main spectrometer.** This block diagram is intended to give an overview of the high voltage setup at the main spectrometer. It includes the setup of the post regulation system that is explained further in section 4.1.4. Details to the precision monitoring of the high voltage, highlighted in gray are explained in section 4.2. The pink colored lines represent a simplified form of the steep and flat cone potentials (described in detail in section 4.1.3). The smoothing capacitors on the left side of the main spectrometer are installed to reduce AC components with frequencies above 1 MHz. In blue the flux tube of the electrons exiting the pre-spectrometer is indicated.

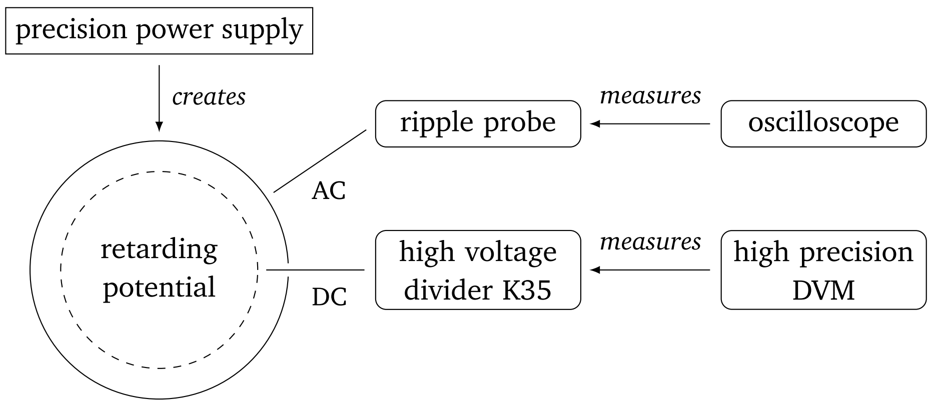

Figure 4c: **Diagram of the high voltage monitoring setup at the main spectrometer.** The monitoring is divided into monitoring the AC component with the ripple probe (element of the post regulation) and monitoring of the DC component using a high voltage divider. The circle symbolizes the vessel potential created by the precision power supply. Together with the IE common power supply this creates the retarding potential (dashed circle).

On the other hand it is essential to monitor voltage deviations. As specified in the KATRIN design report (Angrik et al. 2005) voltage deviations up to 3 ppm, that equals 60 mV at 18.6 kV are allowed.

The following sections will present the monitoring of the high voltage at the main spectrometer. Figure 4c shows the basic monitoring scheme divided into monitoring of AC and DC component as it is in place at the main spectrometer.

4.2.1 Monitoring of AC Component

The *ripple probe*, an element of the post regulation (explained in section 4.1.4) is used to monitor the AC component of the high voltage on the main spectrometer. The ripple probes signal can be recorded with an oscilloscope.

The recording of the ripple probes signal can be done continuously during measurements. Readout of the oscilloscope is done manually for selected periods of time. This can be used to verify the functionality of the post regulation setup, but also to check the ripple during times when the active post regulation setup is not used.

Figure 4d shows an example of the ripple probe signal readout by an oscilloscope, with and without active post regulation. This illustrates the capability of the post regulation to smooth out ripples on the high voltage.

Another example of the ripple probe signal can be found in chapter 7, where the ripple on the high voltage without active post regulation is analyzed in detail.

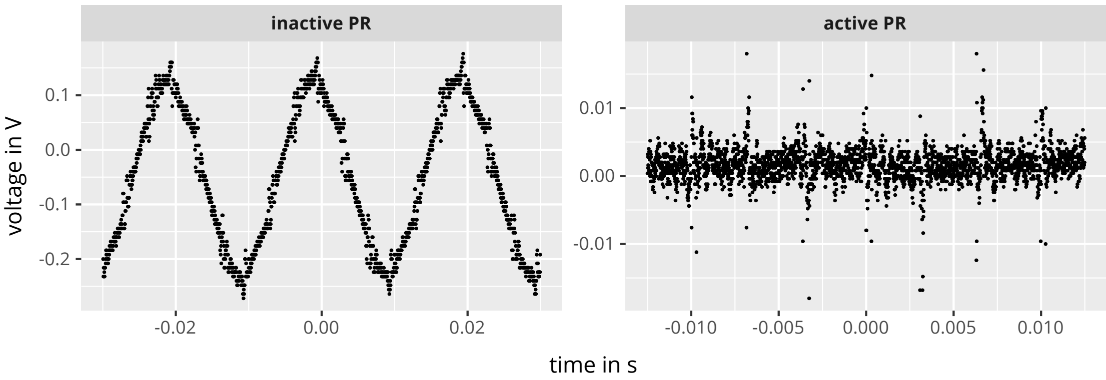

Figure 4d: **Ripple compensation of main spectrometer high voltage with post regulation.** These measurements with the ripple probe show the comparison between active post regulation on the right and inactive post regulation on the left. The typical 50 Hz ripple is pronounced with an amplitude in the order of 0.25 V in the measurement with inactive post regulation. In the right plot one can see the ripple compensation with active post regulation.

4.2.2 Monitoring of DC Component

Measuring a voltage in the order of 20 kV with sufficient precision to determine whether the voltage fulfills its stability requirements of 3 ppm, is not a simple task. Moreover not only the stability needs to be monitored but also the calibration of the measurement device.

Commercial high precision voltmeters exist, but their ideal measuring range for DC voltages is in the 20 V region and therefore is three orders of magnitudes too small.

To solve this challenge the voltage will be scaled down to the measurement range of the precision voltmeters. This can be done using a voltage divider. A voltage divider, in its most basic form consists of two ohmic resistances connected in series (R_1, R_2). With an input voltage U the partial voltage at the second resistor can be described as:

$$U_2 = \frac{U}{R_1 + R_2} \cdot R_2.$$

This illustrates the dependency of the partial voltage on the scaling factor of the resistors.

Two high precision voltage dividers named K35 and K65 were developed for the KATRIN experiment. The K35 a precision high voltage divider for voltages up to 35 kV, installed and used at the main spectrometer, consists of 106 precision resistors with an optimized temperature dependency. To reduce the temperature dependency even further resistors with positive and negative temperature coefficients are matched (Thümmler et al. 2009).

The ratio between input and output voltage (scale factor) of the voltage divider needs to be known precisely. In addition a reliable method to investigate possible drifts of the scale factor is needed. One method uses a primary standard for high direct-current voltages at the PTB. This has been done in cooperation with the PTB and a scale factor of 1972.453(2) was determined (Schmidt, Meisner 2013).

Another method to measure the scale factor was performed during the commissioning measurement phase with ^{83m}Kr. With measuring the difference between conversion electron lines K-32 and L_3-32 of the gaseous ^{83m}Kr source the scale factor can be determined (Arenz et al. 2018b). The obtained scale factor is 1972.449(10). Comparing the results of both methods shows the long-term stability of the K35 scale factor.

The K65 divider was developed to have an additional voltage divider monitoring the high voltage (Bauer et al. 2013). This voltage divider can operate with voltages up to 65 kV.

During calibrations at the PTB in 2013 the K65 exhibited fluctuations of the scale factor up to 20 ppm. Those anomalies were traced back to loose screw connections in the resistor chain (Rest 2014). A simple tightening of the screw connections was not the solution as it damages the connecting wires. Using silver tubes as connection elements proved to be the solution. For this the complete K65 was disassembled and again reassembled with the improved connectors in November 2017 (Rest 2018).

The main spectrometer high voltage can be connected to the monitor spectrometer providing the possibility to monitor the high voltage at the monitor spectrometer (see chapter 3.2.5). As part of this thesis a status display was developed in cooperation with the Institute for Data Processing and Electronics (IPE). Its purpose is to monitor the current high voltage configuration and to simplify operating the monitor spectrometer. A screenshot of the status display is depicted in the appendix in figure Aa.

In addition to the two precision high voltage dividers the monitor spectrometer gives an independent high voltage monitoring. These three devices provide an independent monitoring system that is fail-safe.

Nevertheless to measure the voltages a precision voltmeter is needed. During normal operation of the KATRIN spectrometer voltages around 18 kV are used. Scaling with the K35 creates voltages around 9 V that need to be measured with high precision.

As voltmeter the reference multimeter Fluke 8508A, called DVM-A, is chosen. DVM-A is a 8.5-digit multimeter whose stability and accuracy is designed for calibration laboratories.

For DC voltage measurements in the 20 V range the uncertainty relative to a calibration standard is given as 0.5 ppm/d, with an ambient temperature stabilized to $\pm 1\,^{\circ}\mathrm{C}$ (Fluke 2002).

The multimeter is located in the main spectrometer hall inside a control cabinet. The complete main spectrometer hall is temperature stabilized during measurements, ensuring $\Delta T < 0.5\,^{\circ}\mathrm{C}$. Additionally the control cabinet, where the multimeter is located is equipped with ventilators. This ensures a controlled ambient temperature meeting the manufactor specifications for the multimeter. The calibration and the performance of the multimeter is presented in the next chapter.

To have a fail-safe system, a second multimeter of the exact same type, called DVM-B exists. This secondary multimeter also provides the possibility of crosschecking the behavior of both multimeters, as shown in section 5.3.2.

5 Low Voltage Calibration

In order to use the MAC-E filter as intended (see section 3.1), a reliable voltage monitoring is needed. As described in section 4.2, the voltage divider K35 and the precision multimeter Fluke 8508A (DVM-A) are in place to perform this task.

In order to perform reliable voltage measurements, every multimeter needs to be calibrated. The choice of calibration procedure is dependent on the requirements for the accuracy of the voltage values. To use DVM-A to its full capacity, it needs to be calibrated up to its 8.5 digits. Therefore a dedicated calibration method has been chosen for the calibration of DVM-A.

This chapter introduces the calibration method and discusses the results. Additionally, long-term investigations of the performance of multimeter and reference sources are presented. Afterwards, recommendations based on the demonstrated performance are made regarding calibrations for future measurements.

5.1 Calibration Method and Procedure

The calibration procedure of DVM-A consists of a combined zero-offset and $-10\,\mathrm{V}$ gain measurement. The $-10\,\mathrm{V}$ are chosen because the measurements of the voltmeter during neutrino mass measurements are around $-9\,\mathrm{V}$. They are supplied by five different direct voltage reference standards. One of them is a Fluke 732A and the other four are of type Fluke 732B – hereafter called REF-A and REF-B1 through REF-B4, respectively. The Fluke 732B devices are depicted in figure 5a.

Every calibration measurement – the procedure is visualized in figure 5b – starts and ends with connecting all the measuring lines of the voltmeter to the ground wire in order to apply a voltage of zero to the voltmeter, this is named zero-offset measurement. After the zero-offset measurement the references are connected to the voltmeter with their 10 V outputs – one after another, for about two minutes each.

DVM-A is used in its 7.5-digit fast mode where it has an integration time of 64 PLC that equals 1.28 s at 50 Hz (Fluke 2002). The slow control system (cf. 4.1.1) provides a readout every 4 s. Over a 2 min measurement period this results in 30 data points, providing sufficient statistics within reasonable time. The first offset measurement is set to four minutes to recognize possible systematics early on, and to repeat the measurement if necessary. In

Figure 5a: **Fluke 732B direct voltage standard.** This picture shows the Fluke 734A which consists of four independent Fluke 732B direct voltage reference standards. Each of the four provides a 10 V and a 1.018 V reference output.

mid-November 2017 the readout interval of the voltmeter has been tightened to 2 s, doubling the number of data points and thereby reducing the statistical error of each measurement.

With this procedure, one can calculate the gain factor g as follows:

$$g = \frac{U_{\mathrm{ref}}}{m_{\mathrm{ref}} - c}. \tag{5.1}$$

U_{ref} is the voltage of the 10 V output as measured by a calibration against a Josephson voltage standard[1] at the *Physikalisch-Technische Bundesanstalt* (PTB) in May 2017. The calibration values are listed in table 5c. This calibration will be repeated at the PTB once per year. m_{ref} is calculated as the mean value of the 10 V readouts, and the offset c is calculated as the mean value of the zero-offset readouts.

With the Gaussian propagation of uncertainty one gets the following uncertainty estimation:

$$\Delta g = \sqrt{\left(\frac{u(U_{\mathrm{ref}})}{(m_{\mathrm{ref}} - c)}\right)^2 + \left(-\frac{U_{\mathrm{ref}} \cdot u(m_{\mathrm{ref}})}{(m_{\mathrm{ref}} - c)^2}\right)^2 + \left(\frac{U_{\mathrm{ref}} \cdot u(c)}{(m_{\mathrm{ref}} - c)^2}\right)^2} \tag{5.2}$$

The standard deviation of the data points in the measuring interval is used as an error $u(m_{\mathrm{ref}})$ for m_{ref}, and $u(U_{\mathrm{ref}})$ denotes the uncertainty on the calibration value as specified in more detail in section A.1 together with the error estimation $u(c)$ for the offset.

With this method, the gain of the voltmeter can be determined. The stability as given in the specifications of the voltmeter provided by the manufacturer is 0.5(2) ppm/d and 1.4(2) ppm/90d for an ambient temperature between 20 °C to 25 °C stabilized to ±1 °C (Fluke 2002). This indicates that regular calibrations have to be performed to guarantee a voltage readout with a precision in the sub-ppm range. Additionally it is important to keep

[1] The Josephson voltage standard is based on the Josephson effect which was postulated by B. D. Josephson (1962) and observed by S. Shapiro (1963).

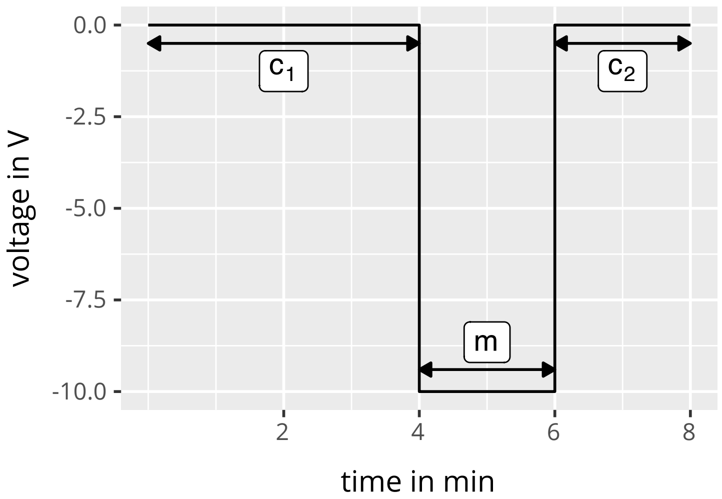

Figure 5b: **Calibration procedure.** This diagram shows the sequence of the calibration procedure with a single reference source. For usual calibrations with multiple reference sources the measurement of m will be repeated for each source. The c_1 and c_2 intervals denote zero-offset measurements, while the m interval denotes $10\,\mathrm{V}$ measurements.

in mind the influence of the ambient temperature on the calibration. Findings of regular calibrations with the described calibration method are presented in the next section.

5.2 Calibration Results

This section will first present the calibration results for the commissioning measurement phase with ^{83m}Kr (see section 3.3). These results show that the presented procedure is able to provide reliable calibrations for the multimeter and therefore offers calibrated voltage values for the analysis of measurements.

To be sure that these results are reproducible for future measurement phases, one still needs to check for possible systematics. Therefore the calibration measurements were continued beyond the comissioning measurement phase and the results are presented in the succeeding sections.

5.2.1 Calibrations for the Commissioning Measurement Phase with ^{83m}Kr

During the commissioning measurement phase with ^{83m}Kr, the calibration measurement was performed every working day to get a close monitoring of the gain.

To calculate the gain of the precision multimeter DVM-A, the gain determined with each reference source is averaged. Details on this method can be found in section 5.2.3. The results for gain and offset are shown in figure 5d.

Experience has shown that due to stable gain values an average over the whole two weeks measurement period is sufficiently precise. Therefore the voltage correction used for analysis of the data taken during these two weeks is

$$U_{\mathrm{cal}} = (U - c) \cdot g = \left(U - 2.9(4) \cdot 10^{-6}\,\mathrm{V}\right) \cdot 0.999\,999\,2(2). \tag{5.3}$$

Details on the error estimation can be found in section A.1.

5.2.2 Review of the Calibration History

Calibration measurements are performed on a semiweekly schedule dating back to August 24, 2017. Before that date, measurements were for the most part only being performed sporadically – an exception being the month of July with measurements done on every single working day.

To evaluate the temperature's influence for each calibration, the average ambient temperature during the measurement was taken. The temperature was measured outside the control cabinet of the references and the voltmeter with a temperature sensor at the K35 voltage divider. Additionally long-term measurements during periods with activated and deactivated air conditioning have been performed and will be discussed in section 5.3.

The results of the calibration measurements are shown in figure 5e. Reference REF-A has been moved to another laboratory since September 1, 2017 and has therefore been excluded from the measurements since then. Looking at the results, an overall negative slope is clearly identifiable on the voltage points for each reference source.

At this point one needs to keep in mind that effects observed in these calibration measure-

Table 5c: **Calibration values for the references obtained from the PTB.** Each reference source used for the calibration of DVM-A has been calibrated at the PTB. The calibration results for the 10 V outputs (U_{ref}) and their standard uncertainty multplied with the coverage factor $k = 2$ u(p) (cf. section A.1) are shown in this table.

device	U_{ref} in V	$u(p)$ in V	date of calibration
REF-A	10.000 050 5	$2.0 \cdot 10^{-6}$	May 5, 2017
REF-B1	10.000 080 3	$9.3 \cdot 10^{-7}$	May 5, 2017
REF-B2	10.000 091 2	$1.1 \cdot 10^{-6}$	May 8, 2017
REF-B3	10.000 096 4	$2.0 \cdot 10^{-6}$	May 5, 2017
REF-B4	10.000 087 1	$1.2 \cdot 10^{-6}$	May 5, 2017

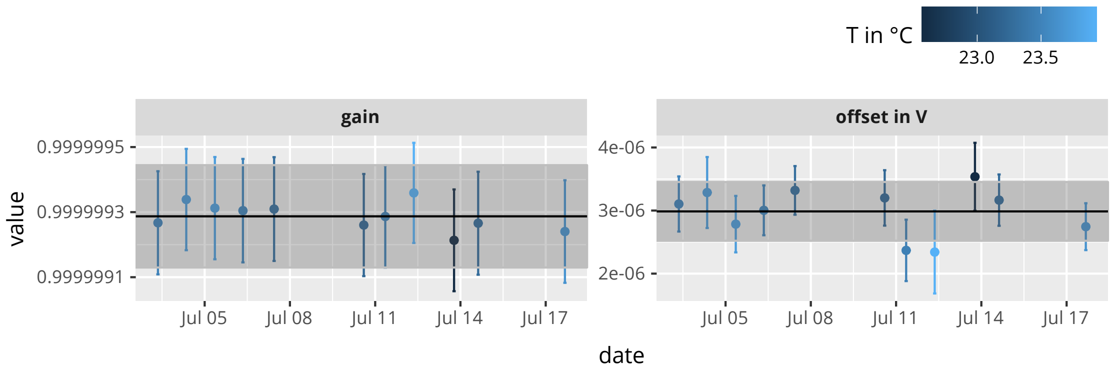

Figure 5d: **Gain and offset for DVM-A during the commissioning measurement phase.** The plot shows the gain and the offset values over the measurement time. Additionally the ambient temperature during the measurement is plotted as color scale.

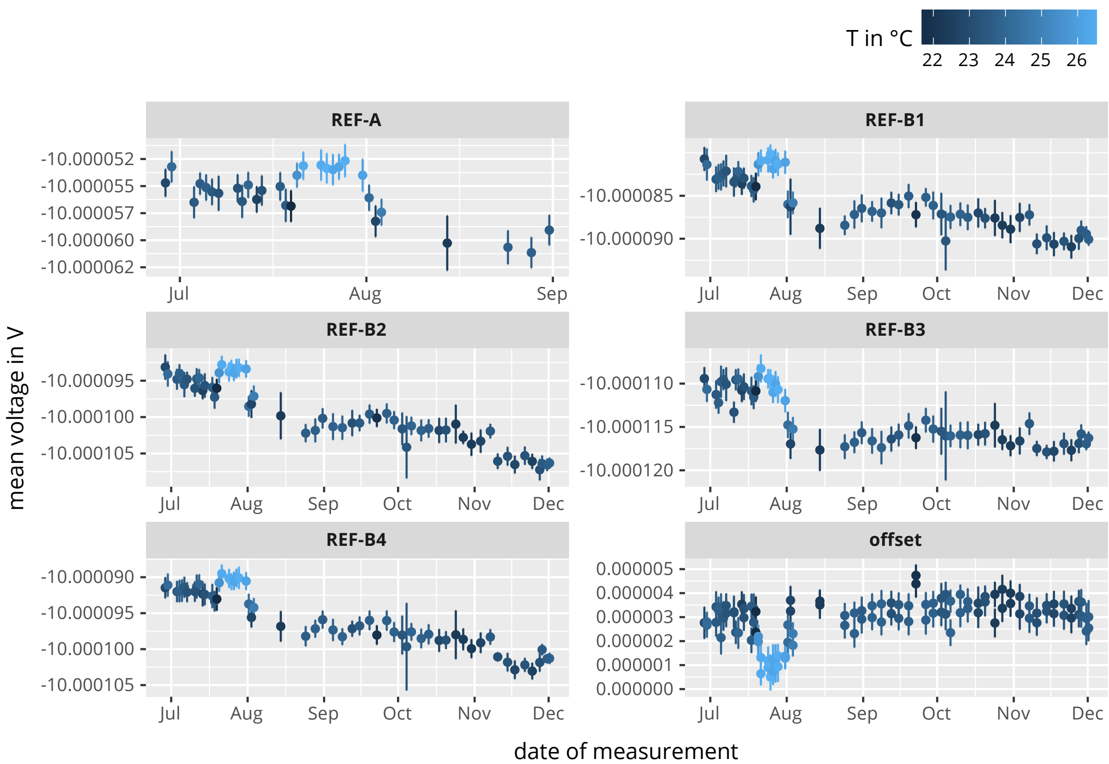

Figure 5e: **Mean voltages of calibration measurements.** The plot shows the development of mean voltages over time. For each data point, the corresponding mean ambient temperature is visible from the color scale. The individual plots show the voltages for the five different reference sources and the zero-offset of the measurement chain.

ments are always a superposition of effects in the voltmeter and in the reference sources – the exception of course being the offset measurement which purely depends on intrinsic properties of the voltmeter.

The almost two weeks of measurements with ambient temperatures above 24 °C stick out from the other measurement points. During this time the air conditioning in the main spectrometer building was shut down. After this period with elevated temperatures, the air conditioning was reactivated again and the temperatures went back to what they were before. The strong influence that the temperatures had on the calibration is apparent. However, there does not appear to be any long-term influence on the offset measurements nor on the reference voltages of the different reference sources.

5.2.3 Gain of Reference Multimeter

For voltage measurements with the voltmeter one needs to have an estimation for its actual gain. Every reference source can in principle be drifting away from the PTB calibration value. For the 732B-type references Fluke specifies the drift as 2.0 ppm in a year (see Fluke 2012, pp. 1–7). To still get an estimation for the gain of the voltmeter the average of each gain determined by the single references is calculated. For this calibration period reference REF-B3 is excluded from calculating the mean as recommended by the PTB. The result is shown in figure 5f.

One can see a temperature dependency of the gain values, the same that was visible in figure 5e. Additionally the gain values exhibit an overall negative slope over time. With linear regression this slope can be approximated as $-0.022(2)$ ppm/30d. At this point it is not discernible whether the slope is caused by the references or the voltmeter. A better assessment will be possible after the second calibration of the reference sources at the PTB, planned for May, 2018.

Still, one can get an estimation of relative drifts of the reference sources amongst each other. For this a linear regression was performed for the voltage measurement values displayed in figure 5e. The results are shown in table 5g. One can see that REF-B3 shows the smallest relative change over time and REF-A together with REF-B2 the largest.

5.3 Investigation of Long-term Behavior

The reference multimeter is used to monitor the analyzing potential as described in chapter 4.2. This means the multimeter will be used continuously during the measurements and therefore needs to have a stable long-term behavior. To investigate that offset measurements

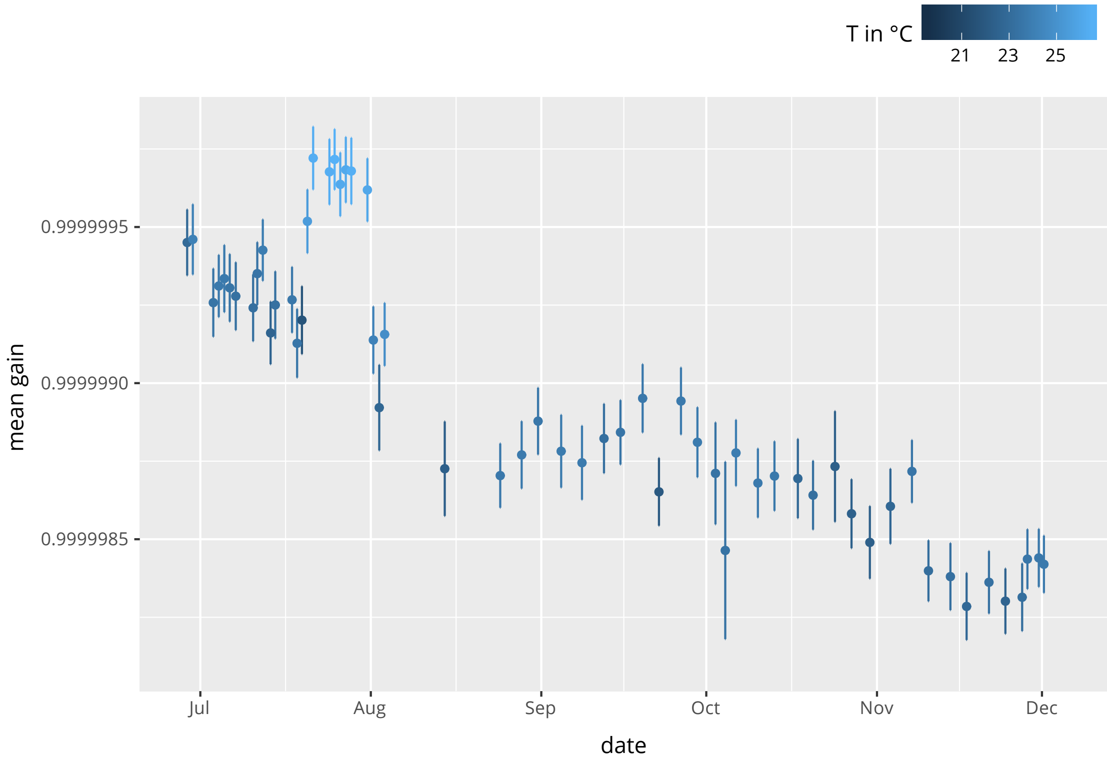

Figure 5f: **Mean gain of reference multimeter DVM-A.** Here the calculated gain for DVM-A is plotted over the date of measurement. The color scale depicts the mean room temperature during the measurement time.

Table 5g: **Relative drift of reference sources.** This table shows the slope obtained by a linear regression of the voltage values over time, displayed in figure 5e. This calculation still includes the additional drift of the voltmeter. Therefore, the values can be used only to make statements of the relative drift between the reference sources.

reference	slope in ppm/30d
REF-A	−0.25(6)
REF-B1	−0.16(1)
REF-B2	−0.24(1)
REF-B3	−0.14(1)
REF-B4	−0.22(1)

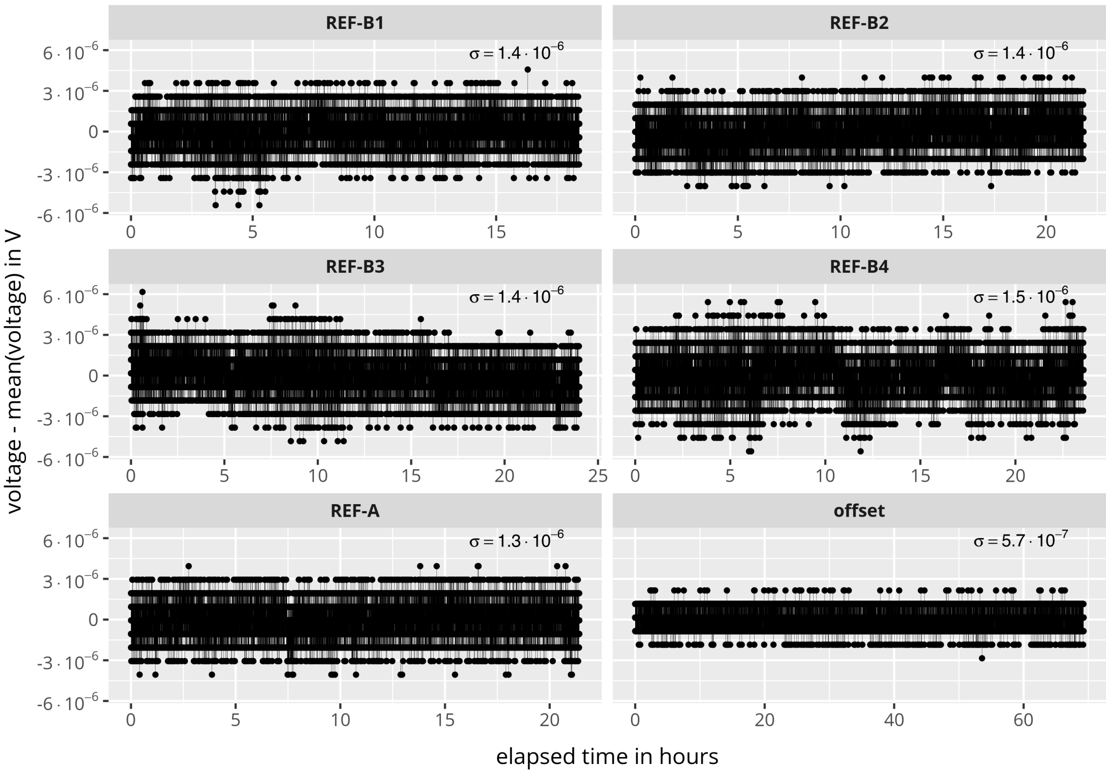

Figure 5h: **Results of long-term measurements with reference multimeter DVM-A.** This plot shows six individual measurements – one offset measurement and five with different voltage reference standards. For each measurement the mean and standard deviation of the voltage values is calculated over the whole measurement time. The difference between each voltage value and the mean is plotted against the elapsed time.

and measurements with the different reference sources have been performed over multiple days. This section will discuss and analyze these measurements.

The first measurement – shown in figure 5h – was taken between July 23, 2017 and July 30, 2017. Each reference source was connected to the voltmeter for roughly one day. The offset of the voltmeter was measured for a weekend. During this time the air conditioning in the main spectrometer hall was deactivated and the temperature was 25.0(5) °C.

To estimate the stability of the measured voltage values the standard deviation over the whole measurement interval is calculated. For the references this is 0.13 ppm to 0.15 ppm and for the offset 0.57 ppm.

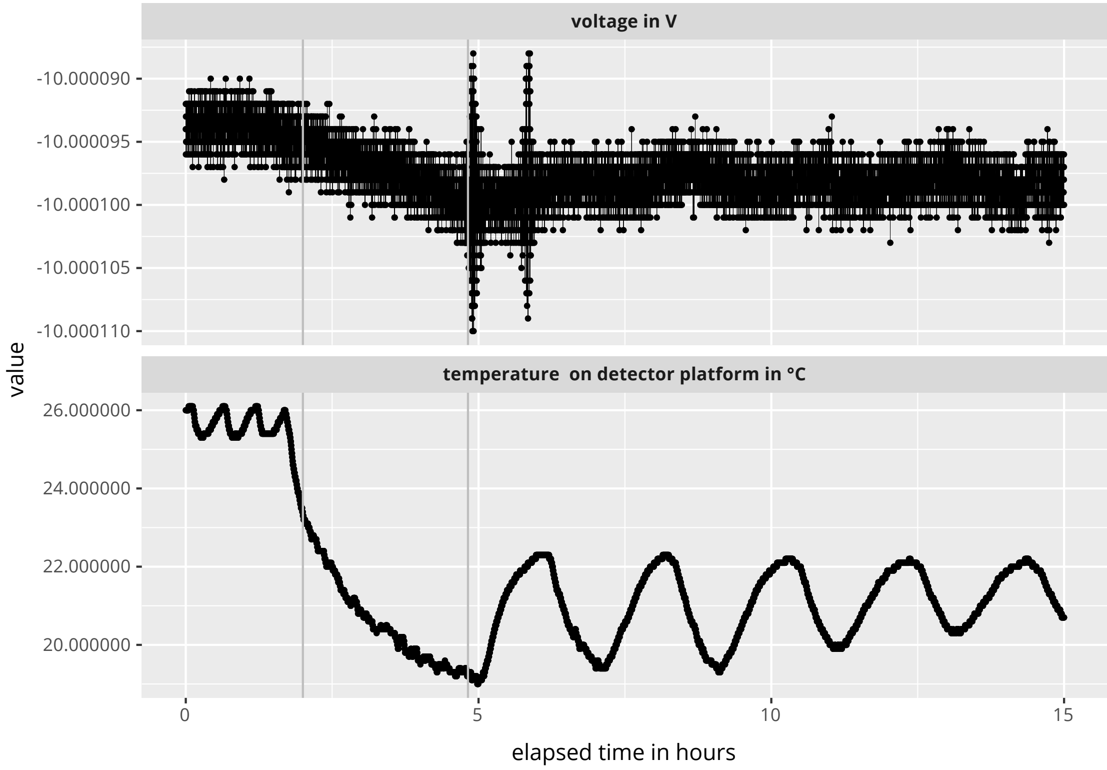

Figure 5i: **Long-term measurement with DVM-A and reference source REF-B2.** Depicted are the voltage values as measured by the reference multimeter DVM-A over the elapsed time. The second plot shows the temperature in the spectrometer hall during the measurement. The gray lines indicate the part of the measurement that is used to calculate a temperature coefficient.

5.3.1 Investigation of Temperature Influences

A second long-term measurement was performed with the reference source REF-B2 (see figure 5i). During this time the air conditioning system was reactivated and the temperature in the main spectrometer hall was cooling down from 26 °C to 20 °C during the measurements.

This measurement can be used to estimate the temperature coefficient of the multimeter. For this the voltages are plotted over the temperatures for the part of the measurement inbetween the gray lines in figure 5i. With this one can estimate the linear temperature coefficient α with:

$$U(T) = U(T_0) \cdot (1 + \alpha(T - T_0))$$

Here $T_0 = 23.3$ °C and $U(T)$ describes the temperature dependency of the voltage. Using

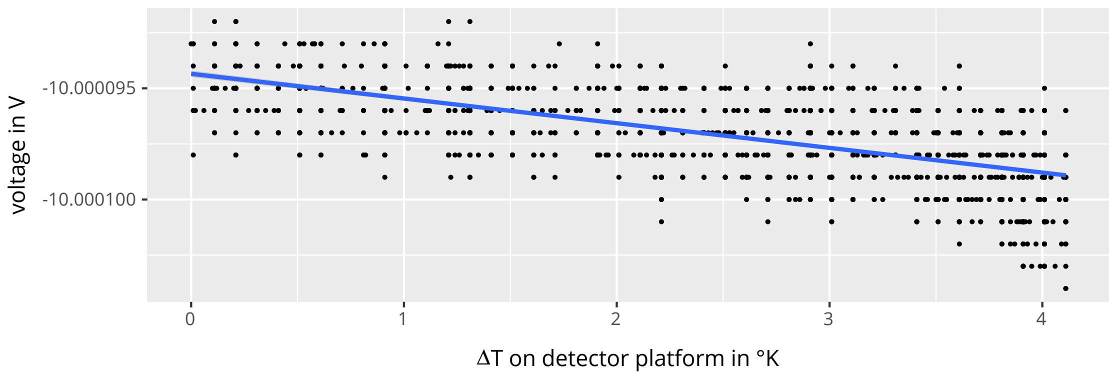

Figure 5j: **Linear temperature coefficient for DVM-A connected to REF-B2.** This plot shows the measured voltage values against the temperature. The blue line shows a linear regression for the measured values.

the slope m and intercept b of a linear regression, as shown in figure 5j:

$$\alpha = \frac{m}{b} \pm \sqrt{\left(\frac{1}{b} \cdot \sigma_m\right)^2 + \left(-\frac{m}{b^2} \cdot \sigma_b\right)^2} \tag{5.4}$$

one gets a temperature coefficient of 0.111(3) ppm/K.

The most noticeable in this measurement are the two spikes in the voltages around 5 h of elapsed time. Observing the temperature changes one can see that at a temperature around 19 °C the air conditioning system stops its active cooling. However the surrounding temperature has not been cooled down that far which causes an abrupt rise in the temperature after the stop of the active cooling. The spikes are at the positions where the temperature is changing rapidly caused by deactivating and activating the active cooling. This indicates that the spikes are a reaction of the voltmeter to the fast temperature changes.

This effect has been also observed at another time with reference source REF-B4 connected to the voltmeter. The results of this measurement are shown in the appendix in figure Ab and figure Ac. Making the same estimation for a linear temperature coeffiecient results in $\alpha = 0.129(3)$ ppm/K, which is in the same order as the one before.

Both long-term measurements clearly illustrate the temperature dependency of the voltage measurements. Especially fast changes in the temperature lead to instable voltage values. Nevertheless, during normal measurement operation in the spectrometer hall, the active temperature stabilization ensures $\Delta T < 0.5$ °C. With the calculated linear temperature coefficients this temperature induces stability uncertainties in the order of 0.07 ppm.

5.3.2 Comparison Between the Two Reference Multimeters

During calibration and long-term measurements DVM-A showed on small timescales stronger fluctuations than usual (spike-like) in the voltages. This can be seen in figure 5i and in figure 5e on October 4, 2017 and October 24, 2017. To investigate this further the backup multimeter DVM-B, which is of the same type as DVM-A is used. DVM-B is positioned in same control cabinet as DVM-A.

With two multimeters of the same kind one can investigate if they show the same behavior. If the spikes would appear simultaneously in both of them one could be sure that they are caused by an external source. On the other hand if it only appears in one of them this could be caused by the multimeter itself or a loose connection.

With both multimeters DVM-A and DVM-B a long-term measurement over almost a month (from November 10, 2017 to December 7, 2017) has been performed. For this measurement DVM-A was connected to reference REF-B3 and DVM-B to REF-BI. The measurement was only interrupted during calibration measurements and one time during check of the electrical safety.

The result is shown in figure 5k. For better visibility the voltage values were summarized hourly. The standard deviation for each hour is then plotted in the second row. Noticeable is the change in the standard deviation from $1.2 \cdot 10^{-6}$ V to $0.9 \cdot 10^{-6}$ V of the DVM-A after the electrical safety check. During this check everything was disconnected and reconnected approximately five hours later. For DVM-B the standard deviation stays the same. The 10 V value changes for both of them and for the DVM-B it is more pronounced and changes about approximately $2 \cdot 10^{-6}$ V.

The overall change in the voltages is stronger for DVM-B than for DVM-A. Here one needs to keep in mind that DVM-B was unboxed and installed just before the measurements. This means the initial, larger changes could have been induced by the multimeter acclimating to the ambient temperature in the control cabinet.

During this measurement the spikes in the voltages only occurred directly after the electrical safety check. In figure Ad those spikes are shown together with the measured values of DVM-B, where they did not appear. Spikes occurred twice (for the second time see figure Ae) shortly after restarting and reconnecting the references. This could be caused by a loose connection, or an internal problem of the DVM-A. At the same time it is improbable that it is some external effect, because then it would have affected DVM-B in the same way.

5.3.3 Influence of Controlled Shutdowns and Power Outages

For an electrical check of the control cabinets, the K35 voltage divider, the multimeters and the references were cut from the power supply for four days. During this time the references

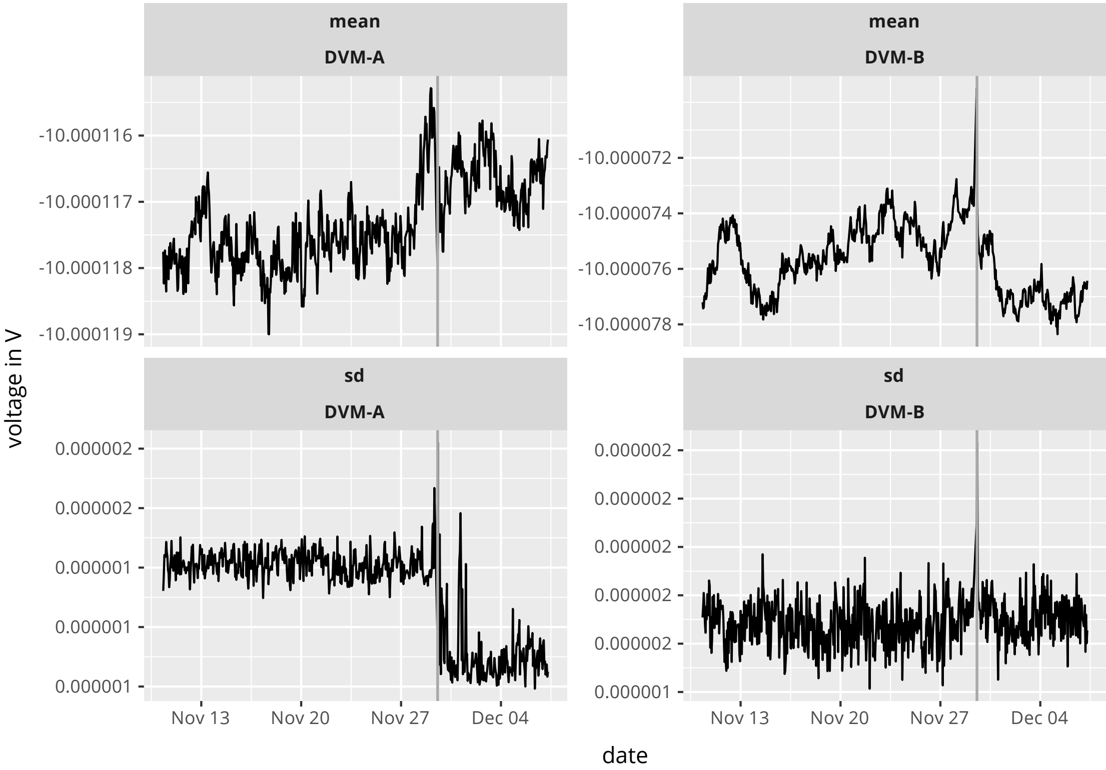

Figure 5k: **Long-term measurement with reference multimeters DVM-A and DVM-B.** The measured voltage points are summarized hourly, the calculated mean and standard deviation for each reference multimeter are plotted against the measurement date. The vertical gray line symbolizes the point where a check for the electrical safety was performed, during which everything was disconnected from the power.

first run on their batteries which then drained whereby the references were shutdown from Sunday to Monday.

Fluke describes a change in the reference voltage outputs due to a power outage without battery support for a duration between 10 min to 24 h as $\leq \pm 0.25$ ppm. The reference sources indicate this possible loss of calibration with extinguishing the "IN CAL" indicator lamp (cf. Fluke 2012).

To get an estimation of the effect of the power outage on the references the measured 10 V values of each reference during the calibrations on December 1, 2017 and December 5, 2017, were compared to the values after the power outage on December 12, 2017 and December 15, 2017. The 10 V values were corrected with the gain of the voltmeter with the same procedure as described in section 5.2.3. The results, listed in table 5l, show a change in the output voltage for all references within between -0.1 ppm to 0.22 ppm, which is within the range of ± 0.25 ppm as specified by Fluke.

This demonstrates that the references output voltages change through power outages but not more than described in their specification. To retain a reliable gain estimation for the voltmeter it should be assured that the reference sources do not lose power.

As discussed in the previous section the effects of the references are superimposed by the effects of the voltmeter. The voltmeter was shutdown during the same time that the reference sources run out of power. Figure Ae shows the running-in characteristic of the voltmeters DVM-A and DVM-B connected to the references REF-BI and REF-B3. One can see a stable voltage measurement with both voltmeters after approximately 9 h.

Calibration measurements after this shutdown show different gain values for the voltmeter than before (see figures Ag and Ah). During the first three measurements the offset of the voltmeter is negative, which has not occurred before. Afterwards the offset is back to normal. One possible explanation for the negative offset could be the deactivated ventilators in the control cabinet, they were reactivated on December 19, 2017. Additionally for further investigations a temperature sensor inside the control cabinet was installed.

Excluding this period during which the offset was negative the gain of the voltmeter differs about $8 \cdot 10^{-7}$ to the gain value before the shutdown.

5.4 Calibration Recommendations for Future Measurement Phases

As shown in the preceding sections, power outages, controlled shutdowns and changes in ambient temperature can change the behavior of references and multimeters.

Linear changes in the ambient temperature can cause a change in the voltage reading of DVM-A in the order of 0.1 ppm/K as shown in section 5.3.1. Therefore the ambient temperature should be kept constant during measurement phases for reliable voltage measurements. If

Table 5l: **Change of reference output voltages due to power outage.** Listed are for each reference the voltage values before and after the power outage. For U_{before} the calibration measurement of December 1, 2017 and December 5, 2017 are used. For U_{after} calibration measurements of December 12, 2017 and December 15, 2017 are used. $\Delta = U_{\text{before}} - U_{\text{after}}$.

reference	U_{before} in V	U_{after} in V	Δ in ppm
REF-BI	−10.000 074(1)	−10.000 073(1)	−0.11
REF-B2	−10.000 095(1)	−10.000 094(2)	−0.11
REF-B3	−10.000 103(1)	−10.000 103(2)	−0.07
REF-B4	−10.000 089(1)	−10.000 092(1)	0.22

there are measurements where this is not the case, these results can give an assessment of the temperature influence on the voltage values.

Section 5.3.3 shows that the behavior of the multimeters as well as the references change if they are restarted. The measurements showed that after a restart one can expect a reliable voltage measurement after approximatly 9 h. During standard operation and especially during measurement phases restarting reference sources or the voltmeter should be avoided. To ensure that, the control cabinet of the voltmeters and reference sources is equipped with an uninterruptible power supply. Additionally each reference source has a battery support which lasts according to their specifications 70 h.

The presented calibration results show that in a controlled environment, the voltage monitoring can be performed in a sub-ppm region. For example, during the two weeks of measurement with ^{83m}Kr the multimeter voltage measurement exhibited a stability of 0.01 ppm as shown in equation (5.3).

For future measurements regular calibrations two times a week are a reasonable effort to ensure reliable voltage readings. If there are indications of strong temperature fluctuations or if electrical safety checks need to be performed as described in the previous section, the calibration measurements should be performed daily until the system is stable again.

6 High Voltage Anomalies During Commissioning Measurements

The commissioning measurements with $^{83\mathrm{m}}$Kr (cf. section 3.3) provided a test of the complete high voltage system under real measurement conditions. Amongst other things it offered an insight into the measurement data volume that accumulates during measurements. All this data needs to be evaluated carefully to ensure reliable analysis.

For the high voltage monitoring, one of the most important sensors is the voltage reading of the voltmeter connected to the high voltage divider K35 (cf. section 4.2). Based on this voltage reading, an automated high voltage quality analysis to distinguish clean and stable runs from those with high voltage anomalies was developed and applied.

This chapter begins with an introduction and description of the high voltage quality filter. It is followed by an investigation of the anomalies discovered using the filter.

6.1 Description of High Voltage Quality Filter for Anomaly Detection

Within the KATRIN collaboration the analysis toolkit BEANS has been developed by S. Enomoto. BEANS provides a variety of tools to analyze and process focal plane detector and slow control data (Enomoto 2017a). Within the BEANS framework it is possible to implement data quality filters (Enomoto 2017b). This was used to analyze the high voltage quality during the $^{83\mathrm{m}}$Kr commissioning measurement phase. For this the examples given in the BEANS Cookbook (http://katana.npl.washington.edu/∼sanshiro/) were adapted for the high voltage requirements.

For most slow control sensors of the KATRIN experiment the data quality analysis can be performed on average sensor values. BEANS provides for example implementations of *auto regressive moving average model* (ARMA) filters to analyse and to evaluate time series data of slow control sensors.

In oder to measure a $^{83\mathrm{m}}$Kr conversion electron spectrum the spectrometer needs to scan from energies below the selected conversion electron line and above. Details to the scanning strategies can be found for example in (Machatschek 2016). Scanning over energies always equals for KATRINs main spectrometer setting the spectrometer vessel on different retarding potentials, as described in chapter 4.

Each measurement period with the focal plane detector is categorized into runs, which themselves are again split into sub-runs. One run is defined by a start and end time. The control of run and sub-run is executed by the focal plane detector measurement and data acquisition software, called ORCA.

The active changing of the voltage during runs offers a challenge to the data quality analysis. Using the derivative of the voltage reading by the K35 proved to be a solution. The associated code for the high voltage quality filter is shown in listing Ai in the appendix.

The BEANS processor `KDTimeSeriesTwoPointDerivativeProcessor` is used to calculate the derivative. Input for the processor is a `KDTimeSeries` read in with the `KDTimeSeriesSlowControlReadoutProcessor`.

For each sensor value the processor calculates the difference to its predecessor sensor value. This difference is then divided by the time difference between the time stamps corresponding to the sensor value and its predecessor, resulting in δv. This time difference is added to the time stamp corresponding to the sensor value, resulting in $t + \delta t$. A new time series tuple consisting of δv and $t + \delta t$ is formed. This creates a time series that is a numeric derivative of the original time series.

The derivative values are then processed with another BEANS processor called `KDTimeSeriesValueAlertProcessor`. This processor enables to define alert levels for the derivative values.

During the measurements the maximum allowed ramping speed of the voltage power supply was restricted to 50 V/s. The internal maximum value for ramping speed of the voltage power supply is 500 V/s. The chosen voltage steps during one run are usually smaller than 1 V. These constraints can be used to define three types of alert levels:

- alert level 10: $\frac{\Delta U}{t} \geq |10\,\mathrm{V/s}|$ indicates an unusual line scan.
- alert level 50: $\frac{\Delta U}{t} \geq |50\,\mathrm{V/s}|$, indicates behavior that is possible during normal operation of the power supply, but has been restricted during measurements.
- alert level 100: $\frac{\Delta U}{t} \geq |500\,\mathrm{V/s}|$, indicates behavior that is not possible during normal operation of power supply.

The high voltage quality filter was applied on all runs during the $^{83\mathrm{m}}$Kr measurement phase and on an excerpt of runs during the spectrometer commissioning measurement phase, called SDS3. Every run with an alert level unequal zero was investigated and categorized. The three main categories of voltage anomalies that result out of this investigations are presented and discussed in the following sections. Runs associated with these categories are shown together with the alert level in the tables Ak - Am in the appendix.

An extension for this high voltage quality filter would be to use it for stability analysis. Here the focus would not be on the derivative of the high voltage values but on the mean and standard deviation. For this to work, first the time periods during which the voltage setpoint was kept constant need to be identified. Up to now a simple way to identify those time periods still needs to be implemented. Inside these time periods one could then investigate the mean value and the standard deviation of the sensor values. For this one could use the *moving average* processor, also provided by BEANS, and make an automated high voltage stability analysis possible.

6.2 Missing Sensor Reading

There are two reasons for missing sensor readings for the voltage divider voltmeter. The first one is the calibration of the voltmeter. During this time the voltmeter is disconnected from the voltage divider and therefore the monitoring of the spectrometer voltage is interrupted. As discussed in the previous chapter, calibrations will be perfomed twice weekly and have a duration of about 20 min.

The second reason are sensor errors where sensor readings are zero for one or multiple values. An example for this is shown in table 6a. During the time period depicted in the table voltmeter DVM-A was connected to reference REF-B3 and DVM-B to reference REF-BI. It is very unlikely that both references interrupt the 10 V input at the same time.

Table 6a: **Missing Sensor Readings for the K35 and K65 voltmeters.** This table shows the sensor readings (in V) of the K35 voltmeter (DVM-A) and the K65 voltmeter (DVM-B) on December 1, 2017. Additionally, the values for the trigger times t are listed. The trigger times are in seconds since January 1, 1904. It is apparant that the missing readout occurs simultaneously for both voltmeters and coincides with missing trigger times.

time	U_{K35} in V	t_{K35} in s	U_{K65} in V	t_{K65} in s
21:08:44	−10.000 118	3 595 007 315	−10.000 075	3 595 007 315
21:08:46	−10.000 117	3 595 007 317	−10.000 075	3 595 007 317
21:08:53	−10.000 117	3 595 007 319	−10.000 075	3 595 007 319
21:08:55	−10.000 116	3 595 007 325	−10.000 076	3 595 007 327
21:08:58	−10.000 117	3 595 007 327	−10.000 076	3 595 007 327
21:09:00	−10.000 117	3 595 007 327	−10.000 076	3 595 007 327
21:09:02	−10.000 117	3 595 007 327	−10.000 076	3 595 007 327
21:09:04	0	0	0	0
21:09:06	0	0	0	0
21:09:08	0	0	0	0

Coinciding with the zero voltage readings, the values for the trigger times are zero as well. Shortly before they are zero, the trigger times values stay the same. This strongly points towards a problem in the data acquisition chain. These missing sensor readings happen regularly, and also during times when the vessel is on high voltage, here one can crosscheck with the internal voltage reading of the power supplies, which show that the voltage is certainly not zero.

In the tables Ak to Am focal plane detector runs are listed during which missing sensor reading occured. Over the $^{83\mathrm{m}}$Kr measurement phase during for 19 runs ($\sim$3 % of all runs) sensor errors appeared.

For other sensor readings similiar problems have occured. One example are the current readings of magnets at the spectrometer (Behrens 2017). This is an indication for a problem in the general infrastructure for retrieving sensor data.

Missing sensor readings can be easily filtered and then an estimation of the average sensor value for the time without sensor reading can be done. Therefore missing sensor readings are of low revelance for analysis. Nevertheless the cause needs to be found and eliminated.

6.3 Voltage Peaks at Step Transitions

The spectrum measurements of conversion electrons from $^{83\mathrm{m}}$Kr during the commissioning measurement provided an intensive testing of voltage scanning strategies.

Using the high voltage quality filter described in 6.1 highlighted voltage peaks inbetween voltage steps. At these peaks the voltage measured with the K35 voltmeter lies about 250 mV above or below the setpoint. The internal voltage reading of the power supply also shows this peak in the voltage. An example for this is shown in figure 6b.

The voltage setpoint always deviates on small scales from the internal voltage reading. However the difference between the voltage setpoint and the internal voltage reading changes after a voltage peak inbetween voltage steps. This is also visible in figure 6b.

This type of anomaly occurred 23 times during the $^{83\mathrm{m}}$Kr measurement phase. In tables Ak and Al in the appendix runs with these anomalies are listed. With a rough estimation of the number of voltage steps taken during the measurement phase the 23 steps going wrong correspond to about 0.04 %.

Especially noticeable is that the peaks always appear at certain voltage steps. In addition, it does not seem to be important in which direction the steps are taken. For example during line scans the voltage was switched from −31 850.5 V to −31 850.0 V and back. In both directions a peak of the voltage about 250 V was measured. With the difference that while

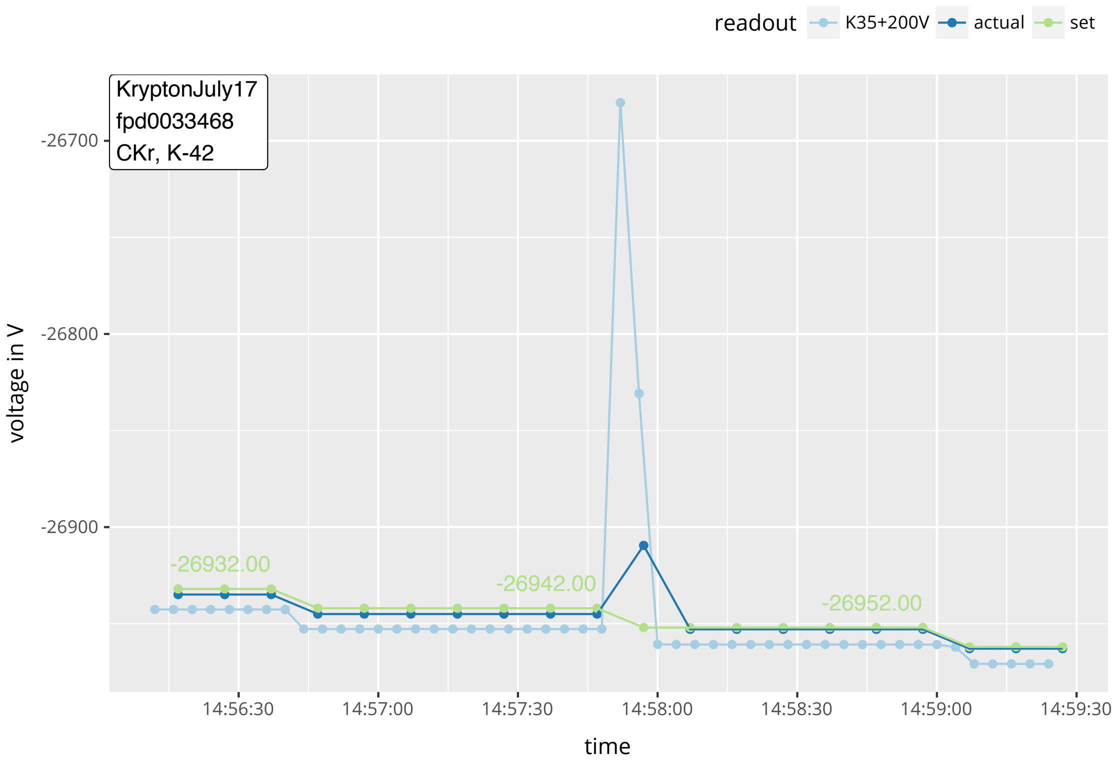

Figure 6b: **Example of a voltage peak at a voltage step.** The sensor reading of the K35 voltmeter is plotted together with the sensor readings – actual (internal voltage reading) and setpoint voltage value – of the precision power supply. For better visibility the K35 voltage was increased by 200 V (corresponds to the IE common potential).

the voltage was increased (absolute values), the peak was above the setpoint. At the voltage step where the voltage was decreased the peak was below the setpoint.

For the analysis of the ^{83m}Kr measurements this high voltage anomaly is of low relevance, as it only appears at the setting of the high voltage. The runs at the FPD are split into sub-runs and for each new setting of the high voltage a new sub-run is started. Therefore these peaks lie inbetween sub-runs.

A possible explanation for this behavior could be a malfunction in the power supply control system. For further investigations of this behavior the programming of the power supplies control system needs to be investigated in detail. In addition dedicated measurements with both power supplies, where the problematic voltage values are set repeatedly are proposed. Testing both power supplies would allow to investigate if the problem is on the controlling side, or if it is an internal problem of the precision power supply (FuG HCP 70M-35000) used during the measurement phase (cf. section 4.1.3).

6.4 Sudden Voltage Drops to Almost Zero

Two times during $^{83\mathrm{m}}$Kr measurements[1] and six times during spectrometer commissioning measurements the precision power supply suddenly dropped from voltages of about 18 kV and 9 kV down to voltages of about 1 kV. After this drop the power supply starts ramping up again with normal ramping speed to its setpoint. The sudden drops in the voltage are not only registered by the K35 voltmeter but also by the power supply's internal voltage measurement.

These sudden voltage drops to almost zero are of high relevance for analysis. It is advisable to exclude runs with these voltage drops. Also an investigation should be perfomed if these voltage drops have a long-term effect on measurements. One idea would be to investigate a change in line positions before and after these incidents. For both incidents, no comparable line measurements were performed close to the incident time, making this investigation impossible with current measurement data.

In figure 6c an example for this sudden voltage drop is shown. Here in addition to the voltmeter reading the readback from the internal values of the power supply is shown.

Coinciding with the voltage drop: the maximum allowed ramping speed drops from 50 V to 0 V. The maximum allowed current drops from 2 mA to 0 mA and the actual current value drops to −1 mA. Additionally, the power supply reading reports an error for the time of the incident.

The incident shown in figure 6c slightly differs from the other as also a change of the internal voltage setpoint value of the power supply occures (changes from 18.5 kV to 18.2 kV). Without a change of the control value of the voltage setpoint.

Another incident with slightly different characteristics occured during run 33522 and is shown in figure An in the appendix. Here the power supply reading only reports an error for the time of the incident, but there are no changes in the other internal sensor values of the power supply.

Because these errors all have slight differences one preliminary conclusion is that the communication with the digital interface of the power supply is defective. The sudden drops in the sensor values can be an indication that the power supply received a reset signal. Every sensor value has a preassigned value to switch to after a reset. For the voltage setpoint the preassigned value is zero.

Up to now the voltage drops to nearly zero only occured for the precision power supply (FuG HCP 70M-35000) and not for the standard power supply (FuG HCN 140M-35000). This points to an internal problem of the power supply or in the communication with the

[1]One incident affected two runs, as it happened at the end of one run.

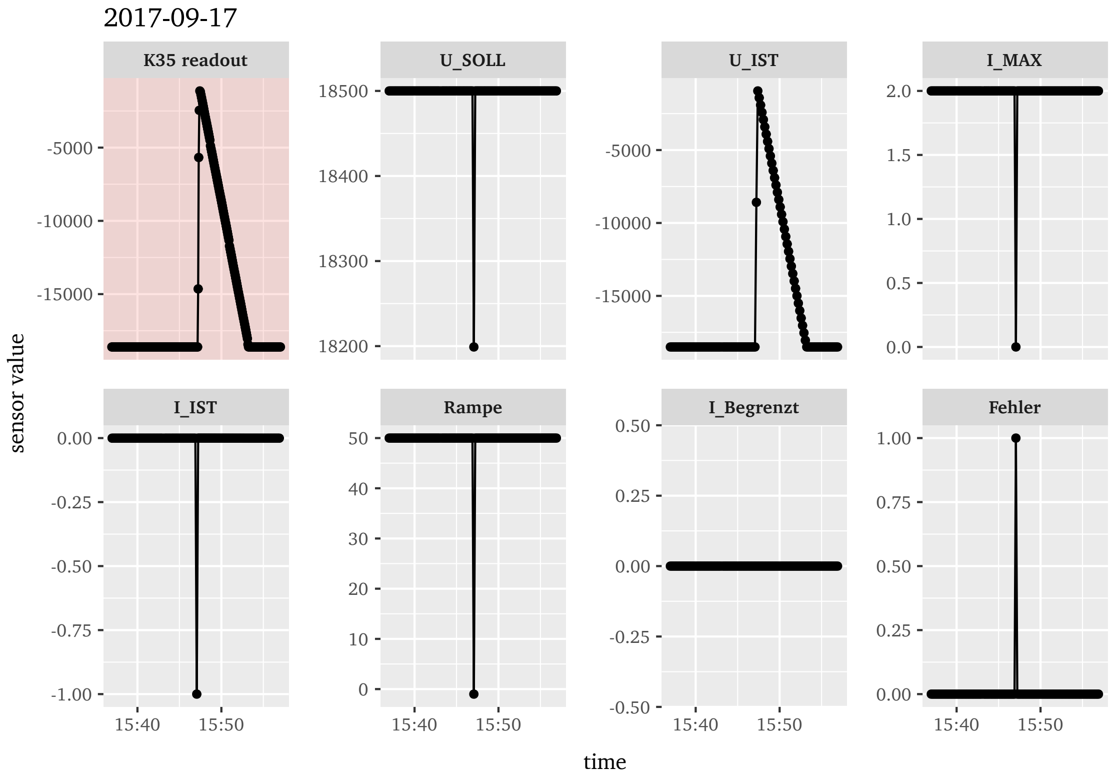

Figure 6c: **Example of a sudden voltage drop to almost zero.** The plot in the upper left, marked in red shows the voltage reading with DVM-A. The other seven plots show sensor readings of the precision power supply over time. One can see that the voltage drop coincides with drops in other values. The mapping of the ADEI sensor identifications used in the plot is listed in table 4a in section 4.1.1.

power supply. This behavior needs to be investigated in the future to ensure a predictable behavior during measurements.

All three kinds of high voltage anomalies presented in this chapter can be identified and measurement runs exhibiting those anomalies can be filtered. This filtering ensures that the high voltage anomalies do not cause mistakes in the analysis. At the same time the high voltage task of KATRIN is working on solutions for the detected anomalies.

7 High Voltage Performance

This chapter reviews the the high voltage performance during the commissioning measurements with $^{83\mathrm{m}}$Kr and begins with an overview of the requirements on the high voltage stability for neutrino mass measurements.

7.1 Influence of High Voltage Stability on Neutrino Mass Measurements

Every measurement exhibits imperfections that give rise to a measurement uncertainty. Those imperfections need to be discovered, classified and if possible reduced to a minimum. Detailed investigations regarding the systematic and statistic effects have been performed for the KATRIN experiment. The overview given in this section is based on (pp. 45ff. Thümmler 2007). It focuses on the influence of the high voltage stability.

During neutrino mass measurements with KATRIN beta decay electrons from tritium are measured. Electrons with kinetic energies close to the endpoint at 18.6 keV carry the most information about the electron neutrino mass, as described in chapter 3.

The statistical uncertainty depends on the scanning range around the endpoint energy E_0. Scanning deep into the beta spectrum can improve the statistical analysis but at the same time increases systematic uncertainties. The interval of $E_0 - 25$ eV to $E_0 + 5$ eV is optimized for high statistics within reasonable systematic uncertainties. This analysis interval gives rise to statistical uncertainties in the order of $\Delta m(\nu_\mathrm{e})_\mathrm{stat} = 0.018$ eV.

The systematic uncertainties should not rise above the statistical uncertainties and therefore are required to fulfill the limit of: $\Delta m(\nu_\mathrm{e})_\mathrm{syst} = 0.018$ eV. Five main systematic uncertainties contributions have been identified. Those contributions are:

1. transmission function and energy loss of electrons inside the WGTS,
2. fluctuations of the tritium column density inside the WGTS,
3. final state distribution of the $(^3\mathrm{HeT})^+$ molecules,
4. elastic scattering of the beta decay electrons with molecules,
5. fluctuations of the absolute energy scale.

Splitting the uncertainty budget among these five contributions gives an upper limit of $\Delta m(\nu_\mathrm{e})_{\mathrm{syst,i}} \leq 0.0075\,\mathrm{eV}$ for each contribution.

Section A.2 gives a detailed derivation of the shift of the electron neutrino mass due to Gaussian distortions of the energy scale. The result

$$\Delta m^2(\nu_\mathrm{e}) \approx -2\sigma^2. \tag{7.1}$$

shows that an energy fluctuation can cause a seemingly smaller neutrino mass value. With the uncertainty budget for fluctuations of the absolute energy scale one can get an upper limit for σ of 0.061 eV.

Given that energy fluctuations are directly connected to high voltage fluctuations this can be transformed to a high voltage stability requirement of 0.61 mV. This translates to a relative stability requirement of 3.3 ppm for the voltages of about 18.6 keV for measurements in the endpoint of the tritium spectrum.

This stability of 3.3 ppm needs to be at least fulfilled over one measurement cycle of up to three months. However this restricts the possibility to investigate systematic effects beyond one measurement cycle.

The high voltage system at KATRIN fullfills these requirements. Investigations estimate the overall high voltage uncertainty at 23 mV. Long-term stabilities of the retarding potential monitored with the high voltage dividers and the monitor spectrometer are better than 1 ppm/60d (cf. p. 135 Kraus 2016).

Calibration measurements for the voltmeter showed a stability of 0.01 ppm for the gain value, over the two weeks commissioning measurements with $^{83\mathrm{m}}$Kr. Together with the continued calibration measurements it becomes apparent that the stability properties of the voltmeter and reference sources only adds a negligible contribution to the uncertainty budget. However this is only justified with continuous calibration measurements of the voltmeter to monitor the reference sources and voltmeter, as described in detail in chapter 5.

7.2 Review of High Voltage Performance during Commissioning Measurements

During the commissioning measurements with $^{83\mathrm{m}}$Kr as described in section 3.3 the high voltage for the retarding potential was primarily set to three different high voltage ranges: 9 kV, 17 kV and 30 kV with the precision power supply (FuG HCP 70M-35000).

To monitor the retarding potential voltage it was connected to the K35 voltage divider and to the monitor spectrometer. Therefore the monitor spectrometer scanned the spectrum of its implanted ^{83}Rb/^{83m}Kr source simultaneously to the scanning at the main spectrometer. Except for the voltage anomalies described in chapter 6 the voltage performance was in its specifications as described in the preceding section.

The inner electrode common potential (IE common) was set to -200 V during the whole measurement phase. This setting needed to be done manually and there was no direct on-line sensor reading during the measurement. Though as described in section 4.2 the K35 divider monitors the retarding potential which is the superposition of vessel and IE common potential. With the patch panel the steep cones of the inner electrode offset were patched to channel 19 and the other offsets were set on the IE common potential. The power supply attached to channel 19 was set to 130 V.

At the time of the measurements the post-regulation loop needed to be disabled for voltages above 20 kV. This was due to partial discharges in the filament heating transformer of the triode shunt regulator (cf. Arenz et al. 2018a). Therefore all of the measurements with the gaseous krypton source were performed without the post-regulation. The same applied to measurements with the condensed krypton source, but here individual measurements with active post-regulations and scanning voltages were performed below 20 kV. Without the post-regulation loop the voltage exhibited an AC interference of 50 Hz (see 4.1.4). This ripple will be investigated in the following section.

7.2.1 Estimation of High Voltage Ripple on Main Spectrometer

To get an estimation of the ripple on the spectrometer during the commissioning measurements the ripple probe of the post regulation was readout with an oscilloscope. This was done three times: one time at 30 kV and two times at 17 kV (called measurement A and B). Every measurement showed a sinusoidal wave-form with an amplitude around 0.2 V.

For the spectral analysis of ^{83m}Kr in the gaseous as well as in the condensed form (see section 3.3) it is important to know as precisely as possible the actual ripple on the voltage, especially to determine the line width properly. If the amplitude of the ripple is overestimated the resulting lines appear smaller than they are in reality and if it is underestimated the line-width appears wider.

The most obvious step to investigate the amplitude of the ripple is to fit a sinus-function to the oscilloscope data. The result of a sinusoidal fit with:

$$f(t) = A \cdot \sin(50\,\mathrm{Hz} \cdot t)$$

is shown in figure 7a for the oscilloscope data taken at 30 kV and in figures Ao and Ar at 17 kV. One can see that this does not represent the actual data. This is confirmed by looking at the residuals, which exhibit a clear structure as shown in figure 7b.

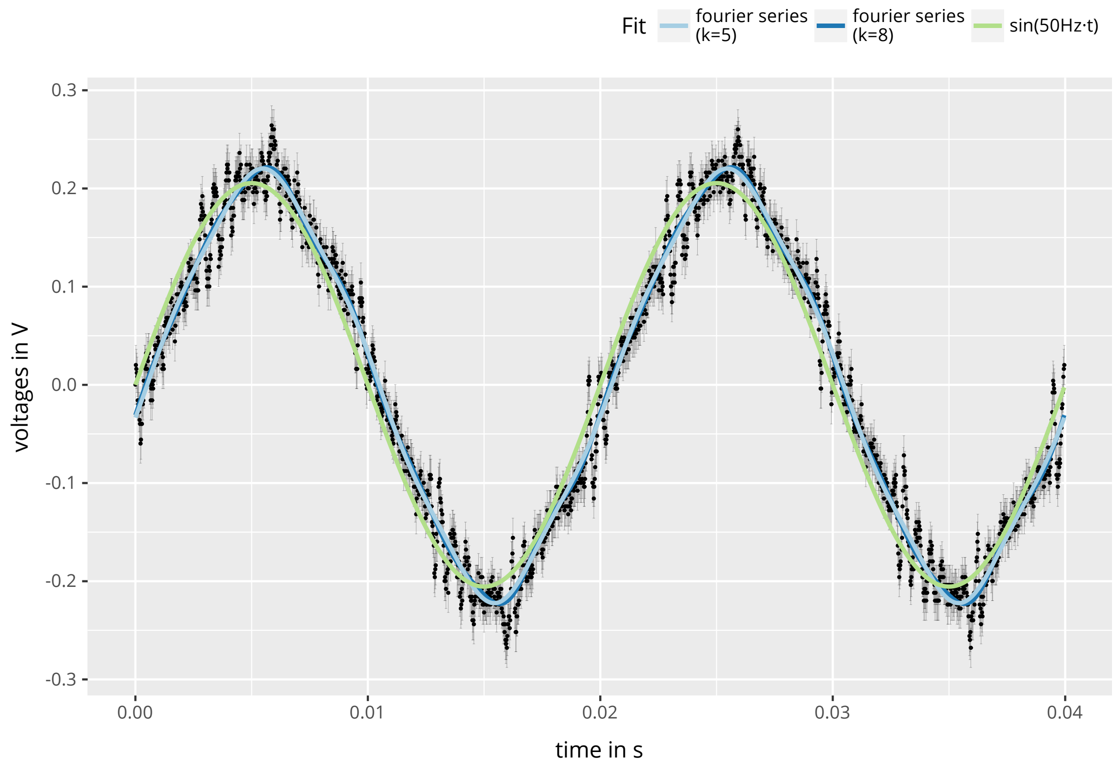

Figure 7a: **Ripple-Probe readout with oscilloscope at 30 kV.** The black dots are the voltage values read from the oscilloscope. The error bars represent an error of $\pm 10\,\mathrm{mV}$ for every voltage point. The three lines show different fits applied on the oscilloscope data.

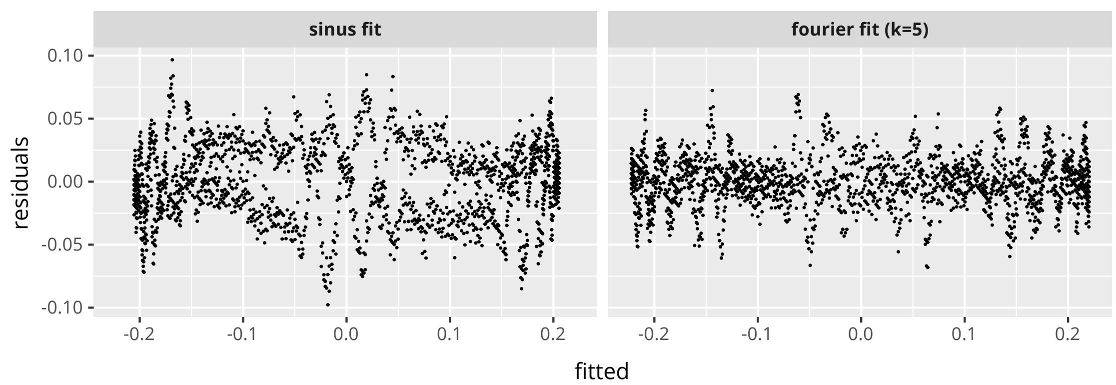

Figure 7b: **Residuals for fits on oscilloscope readout at 30 kV.** The left plot shows the residuals plotted against the fitted values of the sinusoidal fit shown in figure 7a. The right plot is the same for the fit with a Fourier base with $k = 5$.

To get a better estimation of the oscilloscope signal a fit with Fourier base functions has been performed. For this the Fourier series in the form of:

$$f(t) = \frac{A_0}{2} + \sum_1^k A_k \cdot \sin kt + B_k \cdot \cos kt$$

is used. Fits with different k values have been tried and compared. Choosing smaller values for k produces a result that misses the actual structure of the data. At the same time a large k produces overfitting. Using $k = 5$ gives a good description for all three of the oscilloscope readouts. Again the results for this are shown in figures 7a, Ao and Ar. Choosing higher values for k does not provide a significant improvement.

Figure 7b shows the residuals of this fit. They still exhibit a slight structure but are an improvement to the sinusoidal fit. This shows there is still an underlying structure that is not completely understood yet. Still one can use this fit for an estimation of the ripple amplitude:

$$A = \frac{\max(f) - \min(f)}{2}.$$

Here f is the fitted Fourier series.

At this point it is important to mention, that a Fourier base fit is more flexible to possible phase shifts. For example for a sinusoidal structure with a slight phase shift the Fourier base fit adds a higher cosine contribution. The sinusoidal fit is only fitted with an amplitude, not with a phase shift.

Shifting the complete oscilloscope data can also incorporate a phase shift. This improves the sinusoidal fit as shown in figures Ar, As and At in the appendix. However, the sinusoidal fit still underestimates the amplitude. Therefore a Fourier base with with $k = 5$ is chosen to describe the high voltage ripple and to estimate its amplitude.

As uncertainty estimation for the fit, the standard deviation of the residual for each fit was calculated. In figure 7c a histogram with the residuals of the 30 kV measurement is shown, for measurement A and B at 17 kV this is depicted in appendix in figure Aq and At.

For the three measurements this results in amplitudes of

- 0.20(2) V at 17 kV,
- 0.22(2) V at 30 kV.

Another way to estimate the ripple on the high voltage without the active post-regulation system is to look at the rate fluctuations on the FPD count rates. For this kind of measurement to work and to get good statistics one needs to know the fluctuations of the power grid cycles. A device to measure them has already been installed and it is planned to use that for future measurement phases. This will then provide an independent crosscheck for the estimation with the oscilloscope presented above.

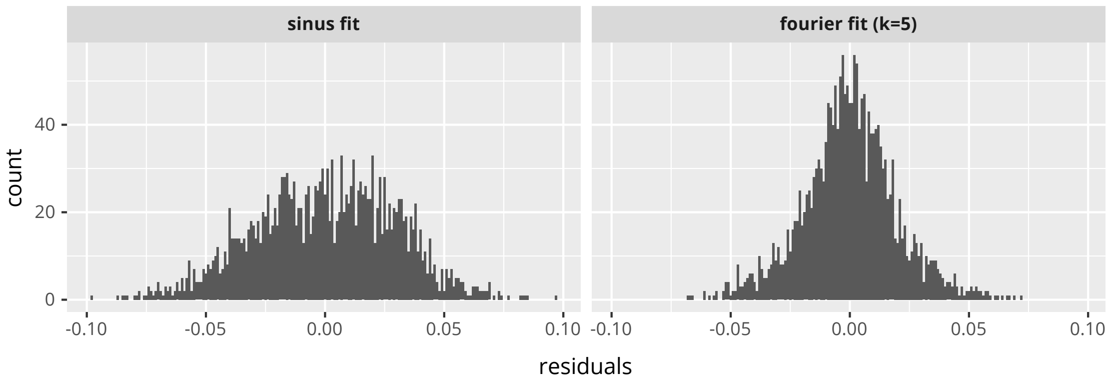

Figure 7c: **Histogram of residuals for fits on oscilloscope readout at 30 kV.** The left plot shows a histogram of the residuals plotted against the fitted values of the sinusoidal fit shown in figure 7a. The right plot is the same for the fit with a Fourier base with $k = 5$. A Gaussian fit for this histogram gives a standard deviation of 0.0297 V for the sine fit, and 0.0198 V for the Fourier base fit.

8 Conclusion and Outlook

The low voltage calibration procedure presented in chapter 5 of this thesis provides a vital foundation for the high voltage monitoring of KATRIN. The calibration measurements need to be continued, with two calibrations per week. Understanding the long-term behavior of the direct voltage standards used as references is essential for a high-quality calibration, and only with an uninterrupted calibration history can that behavior be adequately investigated and evaluated. Additionally, it is advised to perform yearly calibrations of the direct voltage standards at the PTB (*Physikalisch-Technische Bundesanstalt*) to have an additional, independent reference value.

Within the scope of the calibration measurements, the excellent long-term perfomance of DVM-A (Fluke 8508A) has been demonstrated, for example a measurement stability of 0.15 ppm over one day. Investigations have shown that this stability is only achievable when an evenly moderated ambient temperature can be ensured. However, this level of control is possible during measurement phases.

Furthermore, an automated high voltage data quality analysis was developed and applied to the commissioning measurements with conversion electrons of ^{83m}Kr. Acting as a filtering mechanism, the tool makes it possible to evaluate the quality of the high voltage data on a grand scale.

Applying the quality filter to multiple runs (measurement intervals) results in an alert value for each run. A possible expansion of this would be to transform the alert levels to a simpler form: assigning the colors green, yellow, or red to each run.

The voltage values are directly used in the measurement analysis, therefore the data quality is of importance for the high voltage. The quality filter presented in chapter 6 constitutes a big step forward for automated quality analysis of the high voltage data. As a general concept though, this kind of data quality analysis is applicable to every sensor at the KATRIN experiment.

In order to evaluate systematic effects during measurements without the active post regulation system in place, the ripple on the high voltage was investigated. A Fourier base fit with a large sinusoidal contribution proved to be an accurate representation of the high voltage ripple. With this the ripple's amplitudes can be estimated as 0.20(2) V at 17 kV and 0.22(2) V at 30 kV.

For a further investigation, dedicated measurements with conversion electron lines of ^{83m}Kr are proposed. Performing these measurements with and without an active post regulation system, and also with artificial AC noise, will provide a comparision of the ripple inside the spectrometer – as seen by the electrons – with the ripple as seen by the ripple probe of the post regulation system.

All things considered, the monitoring setup of the high voltage system as described in this thesis is ready for neutrino mass measurements with the KATRIN experiment.

Appendix

A.1 Calculation of Measurement Uncertainty for Calibrations

This section shows the calculation of the measurement uncertainty specified in equation (5.3). The calculation is based on GUM (*Guide to the expression of uncertainty in measurement* 1993).

The gain for the voltmeter is calculated as described in equation (5.1) together with the error estimation in equation (5.2). A measurement uncertainty can be estimated for all three components: c, m and U_{ref}.

The uncertainty $u(U_{\mathrm{ref}})$ on the calibration value U_{ref} consists of two elements. One is the uncertainty $u(p)$ as specified on the calibration certificate provided by the PTB. The other element is the knowledge that the reference sources can drift away from this value. This drift $u(d)$ is specified for both reference source types by Fluke in (2012) and (1983). Therefore the uncertainty on the calibration value can be estimated as

$$u(U_{\mathrm{ref}}) = \sqrt{u^2(p) + u^2(d)}.$$

The uncertainty values given by the PTB are a standard uncertainty with the coverage factor $k = 2$. To calculate $u(p)$ the values listed in table 5c need to be divided by the coverage factor.

The stability specified by Fluke for the reference sources is defined for a given period of time at the 99 % confidence level, for three period lengths: 30 d, 90 d and 365 d. The commissioning measurement phase with $^{83\mathrm{m}}\mathrm{Kr}$ ended 74 d after the calibrations done by the PTB. So for this time one needs to take the stability given for 90 d. This specified error needs to be converted to an error value covering the $\pm 1\sigma$ confidence interval. Under the assumption of a normal distribution as Fluke does not indicate the use of a different one, the specified error is divided by 2.58 to obtain $u(d)$

The measurement uncertainty for m, the mean -10 V value measured during the calibration, can be estimated with the standard deviation value: $u(m) = \sigma$.

The same applies to the error estimation for the offset value, with one difference that the offset measurement is done twice (c_1, c_2) and therefore

$$u(\mathrm{c}) = \frac{1}{2}\sqrt{\sigma_{c_1}^2 + \sigma_{c_2}^2}.$$

With this the gain of the multimeter Fluke 8508A during the $^{83\mathrm{m}}$Kr measurement phase can be calculated as:

$$g_{\text{krypton}} = \sum_{\text{meas}}^{11} \left(1/4 \cdot \sum_{\text{ref}} g_{\text{ref}} \pm 1/4 \cdot \sqrt{\sum_{\text{ref}} u(g_{\text{ref}})} \right).$$

In order to get one value for the whole measurement period all eleven measurements are summed up as indicated with the sum over "meas". The index "ref" stands for the four voltage standards used as reference sources: REF-B1, REF-B2, REF-B4 and REF-A.

A.2 Systematic Effects on the Neutrino Mass Due to Gaussian Variations of the Energy Scale

Details to the investigation described in this section are adopted from Thümmler (2007) and Angrik et al. (2005). Near to the endpoint the beta spectrum can be described as (cf. equation 2.3):

$$\frac{d^2N}{dt\, dE_f} \propto (E_0 - E) \cdot \sqrt{(E_0 - E)^2 - m^2(\nu_\mathrm{e})}.$$

Due to the small electron neutrino mass $m^2(\nu_\mathrm{e}) < 2\,\mathrm{eV}$ one can approximate $\sqrt{(E_0 - E)^2 - m^2(\nu_\mathrm{e})}$ with a taylor series at $m^2(\nu_\mathrm{e}) = 0$. This approximation leads to a simplified beta spectrum in the form of

$$\begin{aligned}\frac{d^2N}{dt\, dE_f} &\propto \cdot (E_0 - E) \cdot \left[(E_0 - E) - \frac{1}{2}\frac{m^2(\nu_\mathrm{e})}{(E_0 - E)} + \mathcal{O}\left(m^4(\nu_\mathrm{e})\right) \right] \\ &\approx (E_0 - E)^2 - \frac{1}{2} m^2(\nu_\mathrm{e}) \equiv g(E). \end{aligned} \tag{1}$$

An experimental broadening of the energy can be described with a Gaussian noise, with a standard deviation σ and a mean value $\mu = 0$:

$$f(x) = \frac{1}{\sigma\sqrt{2\pi}} \cdot \exp\left(-\frac{x^2}{2\sigma^2} \right).$$

To estimate the influence of the broadening the beta spectrum in its simplified form $g(E)$

described in equation (1) is convoluted with the Gaussian. Here $a = \frac{1}{2\sigma^2}$ is used.

$$\begin{aligned}
(f * g)(E) &= \int_{-\infty}^{\infty} f(x) \cdot g(E-x)\mathrm{d}x \\
&= \frac{1}{\sigma\sqrt{2\pi}} \int_{-\infty}^{\infty} \exp\left(-ax^2\right) \cdot \left[(E_0 - E - x)^2 - \frac{1}{2}m^2(\nu_\mathrm{e})\right] \mathrm{d}x \\
&= \frac{1}{\sigma\sqrt{2\pi}} \int_{-\infty}^{\infty} \Big[x^2 \cdot \exp\left(-ax^2\right) + (E - E_0) \cdot x \cdot \exp\left(-ax^2\right) + \\
&\qquad\qquad (E_0 - E)^2 \cdot \exp\left(-ax^2\right) - \frac{1}{2}m(\nu_\mathrm{e}) \cdot \exp\left(-ax^2\right)\Big]\mathrm{d}x \\
&= \frac{1}{\sigma\sqrt{2\pi}} \left[\frac{1}{2}\sqrt{\frac{\pi}{a^3}} + 0 + (E_0 - E)^2 \cdot \sqrt{\frac{\pi}{a}} - \frac{1}{2}m^2(\nu_\mathrm{e})\sqrt{\frac{\pi}{a}}\right] \\
&= \sigma^2 + (E_0 - E)^2 - \frac{1}{2}m^2(\nu_\mathrm{e})
\end{aligned}$$

Comparing this to $g(E)$ shows that adding a Gaussian noise to the energy creates a shift in the electron neutrino mass result of

$$\Delta m^2(\nu_\mathrm{e}) \approx -2\sigma^2. \tag{2}$$

This result can be used to estimate an upper limit for the high voltage stability uncertainty (see section 7.1).

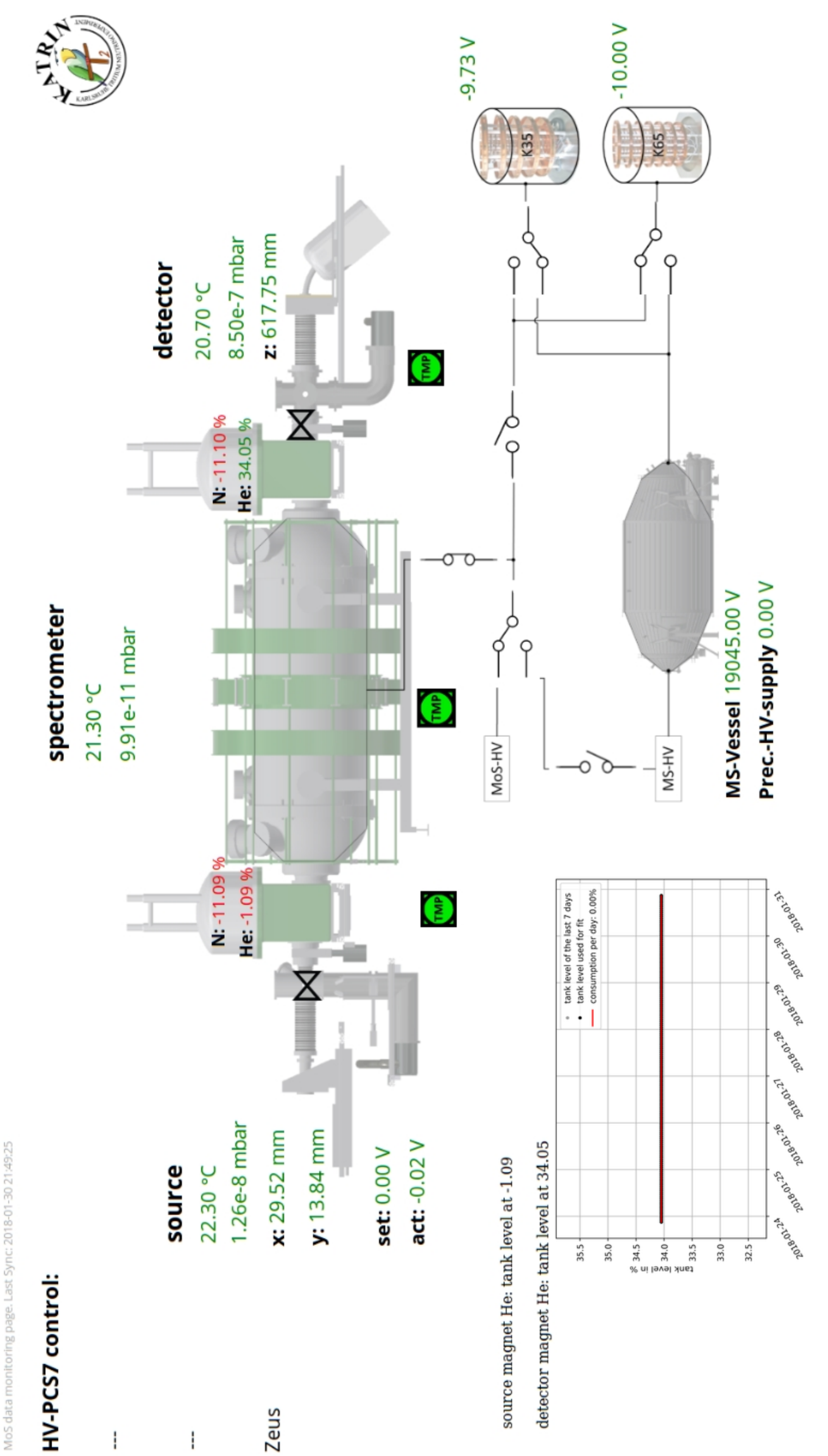

Figure Aa: **Status display for Monitor Spectrometer.** Available at: http://katrin.kit.edu/status/mos/.

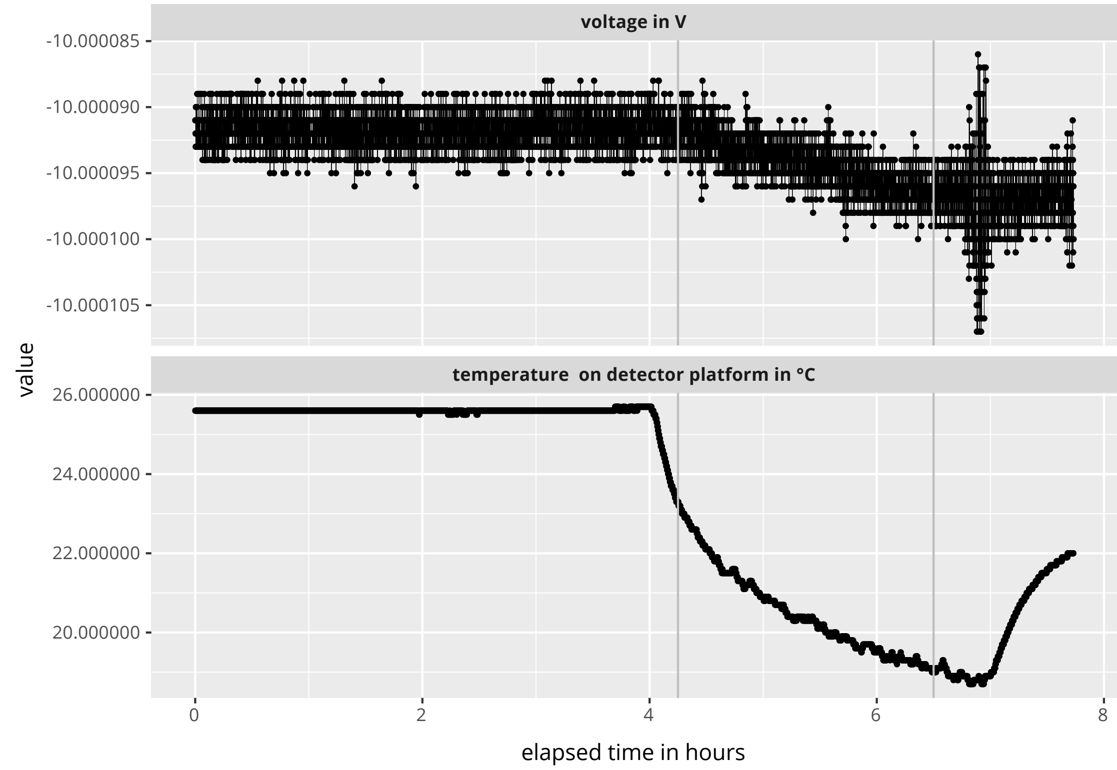

Figure Ab: **Long-term measurement with DVM-A and REF-B4.** Depicted are the voltage values as measured by the multimeter over the elapsed time. The second plot shows the temperature in the spectrometer hall during the measurement. The gray lines indicate the part of the measurement that is used to calculate a temperature coefficient.

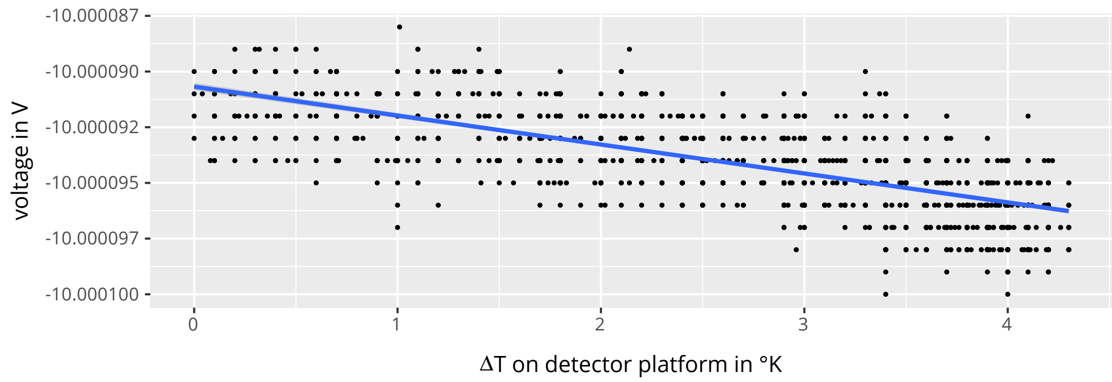

Figure Ac: **Linear temperature coefficient for DVM-A connected to REF-B4.** This plot shows the measured voltage values against the temperature. The blue line shows a linear regression for the measured values. Using the results of the linear regression and equation (5.4) estimates the temperature coefficient as $0.129(3)\,\mathrm{ppm/K}$.

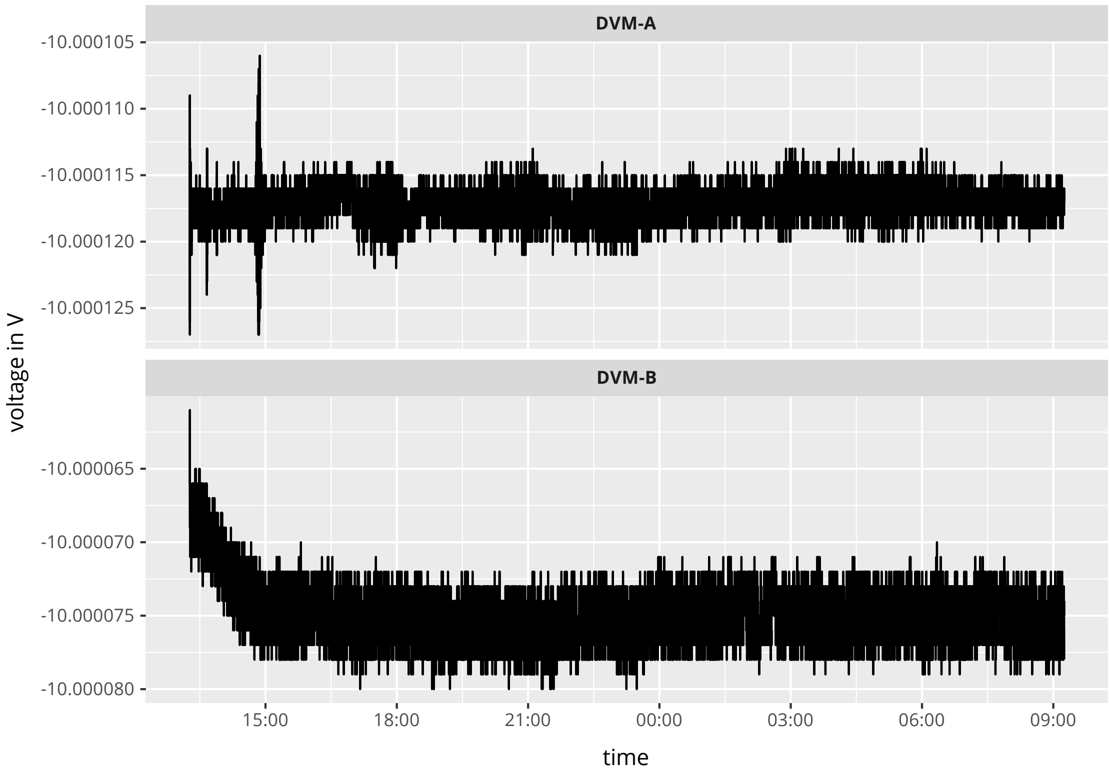

Figure Ad: **Spikes in voltage measurement with multimeter DVM-A.** This plot shows the voltages measured directly after restarting the multimeters DVM-A and DVM-B and reconnecting them to the references REF-B1 and REF-B3 respectively.

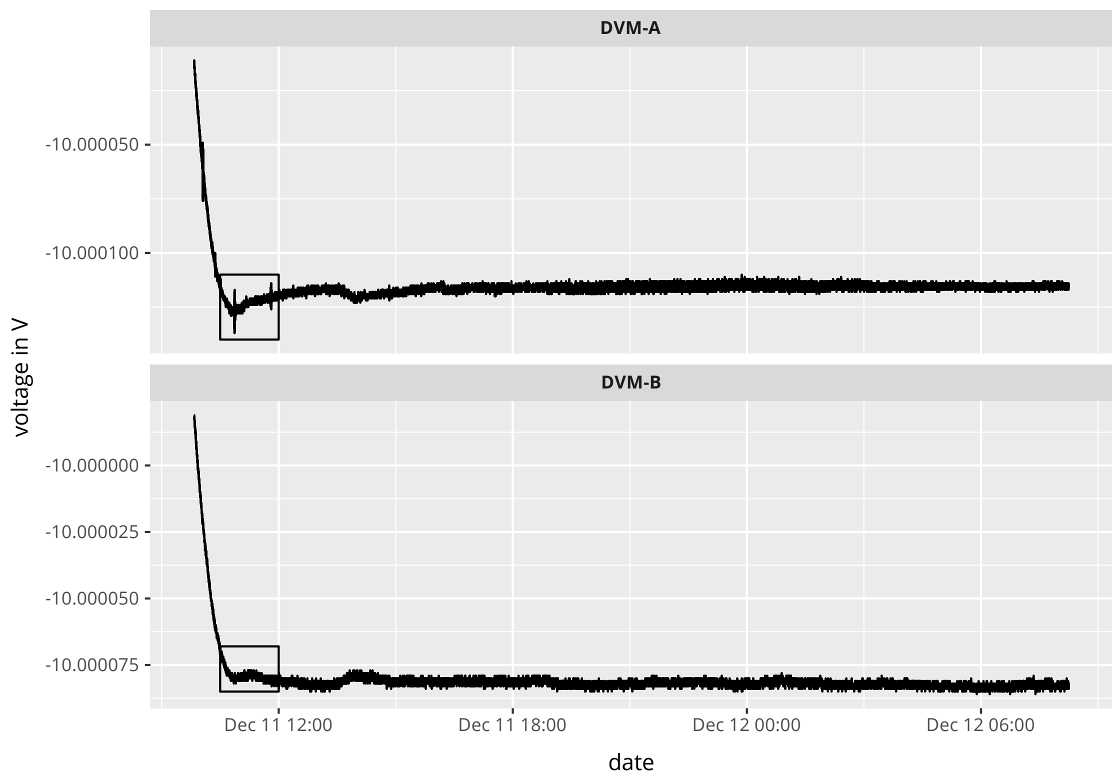

Figure Ae: **Running-in characteristic of DVM-A and DVM-B and reference sources.** This plot shows the characteristics of DVM-A and DVM-B and the reference sources REF-BI and REF-B3 connected to them. The upper plot shows the voltage values for DVM-A and the lower one for DVM-B. The region marked with a rectangular is shown in more detail in figure Af.

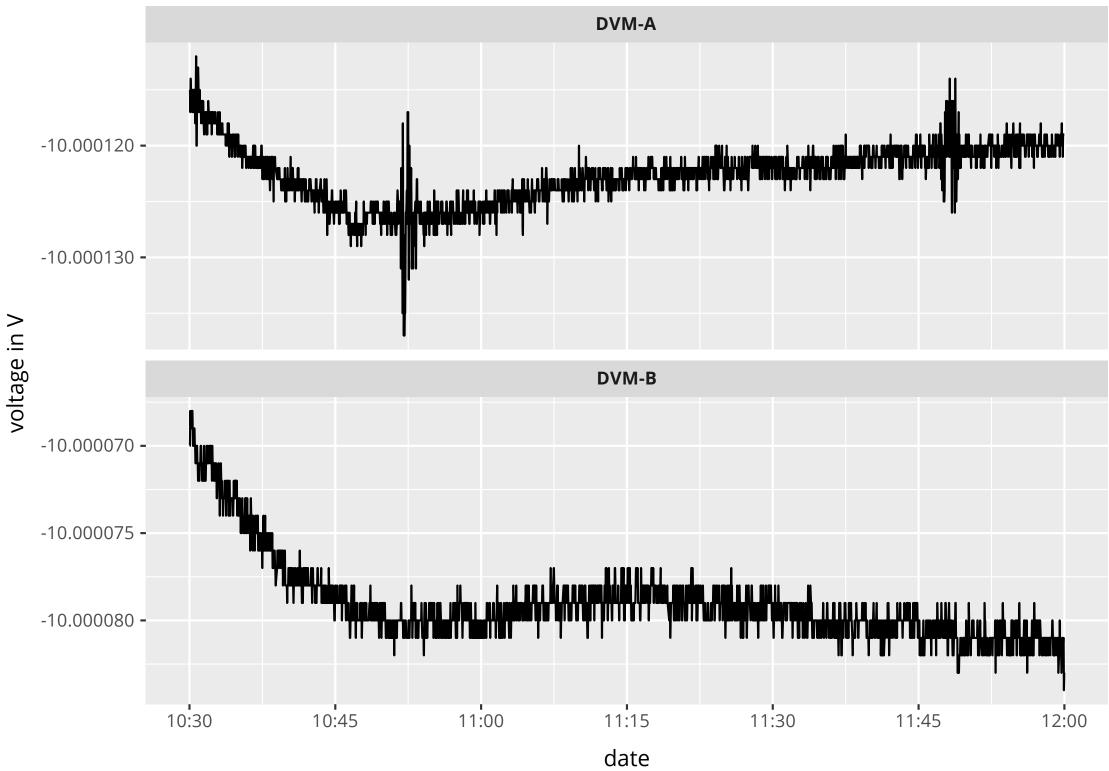

Figure Af: **Voltage spikes in measurements with DVM-A and reference sources.** This plot shows the zoomed region marked in Ae.

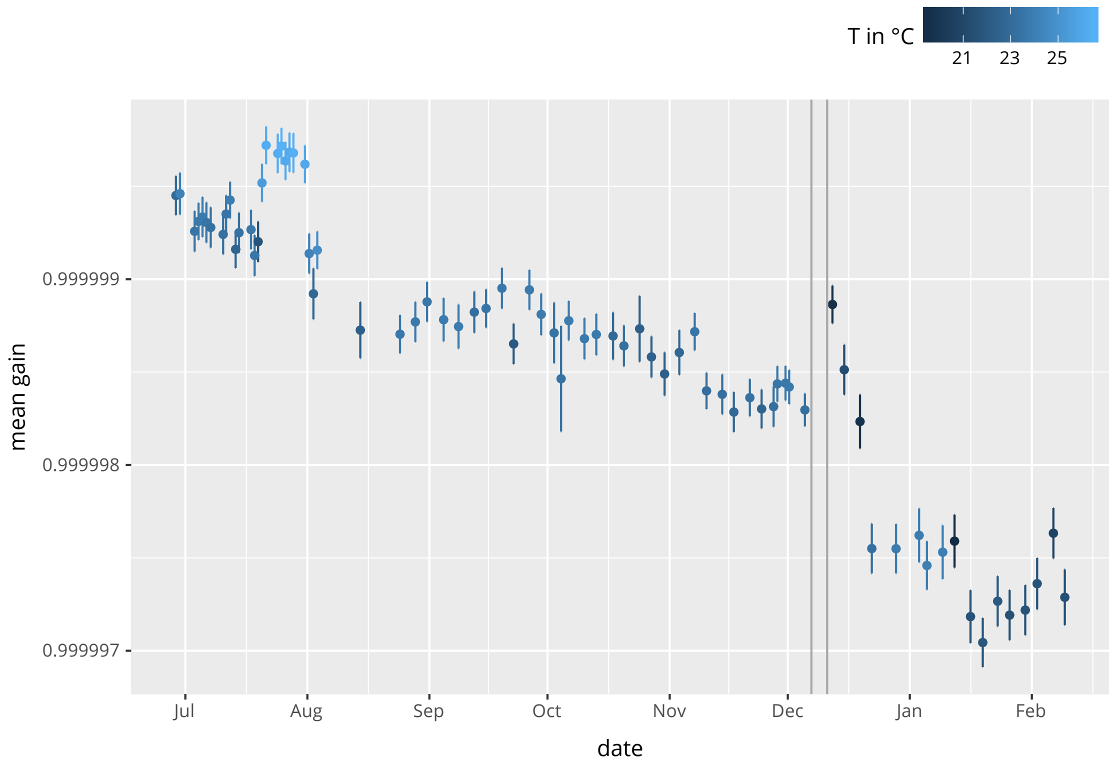

Figure Ag: **Mean gain of reference multimeter DVM-A, full calibration history.** Here the calculated gain for DVM-A is plotted over the date of measurement. The color scale depicts the mean room temperature during the measurement time.

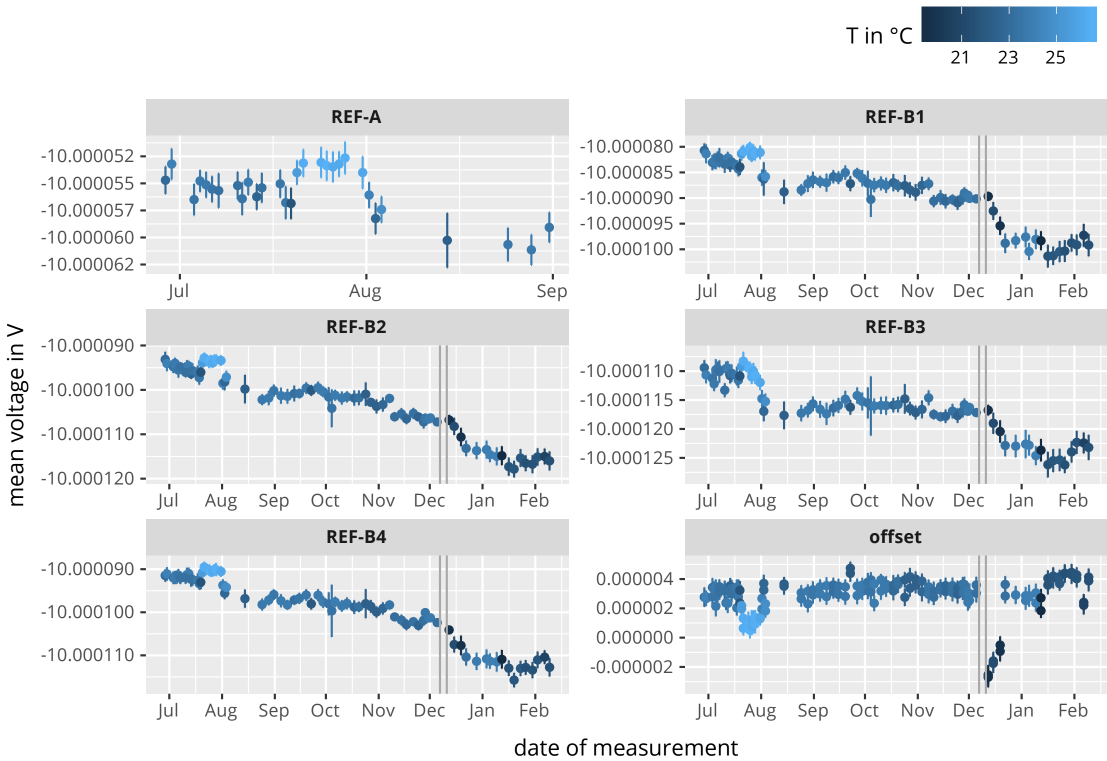

Figure Ah: **Mean voltages of calibration measurements, full calibration history.** The plot shows the development of mean voltages over time. For each data point, the corresponding mean ambient temperature is visible from the color scale. The individual plots show the voltages for the five different reference sources and the zero-offset of the measurement chain.

Listing Ai: **BEANS source code used for the high voltage quality filter.** This is a modified version of the quality analysis examples from the BEANS Cookbook. The implementation is adjusted for the requirements of the high voltage data quality analysis during ^{83m}Kr measurements.

```
#include <KDBeans.h>
#include <fstream>

using namespace std;
using namespace katrin;

int main(int argc, char** argv)
{
  KDBeans beans;

  (beans
    .Append((new KDQualityAnalysis())
        ->SetName("K35")
        ->SetContextLength(5)
        ->AppendProcessor((new KDTimeSeriesSlowControlReadoutProcessor())
            ->SetKatrinNumber("436-REU-0-0201-0001")
          )
        ->AppendProcessor((new KDTimeSeriesTwoPointDerivativeProcessor()))
        ->AppendProcessor((new KDTimeSeriesValueAlertProcessor())
            ->AddLimits(/*AlertLevel*/10, /*Lower*/-10, /*Upper*/10)
            ->AddLimits(/*AlertLevel*/50, /*Lower*/-50, /*Upper*/50)
            ->AddLimits(/*AlertLevel*/100, /*Lower*/-500, /*Upper*/500)
          )
        ->AppendProcessor((new KDTimeSeriesAlertTimeExtensionProcessor())
            -> SetLength(10)
          )
        ->StoreProcessorOutput()
     )
    .Append((new KDTimeSeriesStatistics())
        ->AddInputNameRegex(".*\\.ValueAlert"))
    .Append(new KDRunParameterDump())
  );

  beans.Build(argc, argv).Start();
  return 0;
}
```

Listing Aj: **Shell script for generating alert level summaries.** This script was used to scan over a selected range of runs to generate a list of all runs with non-zero alert levels. It uses the BEANS quality analysis presented above, here called `HV-quality-first-filter`.

```
#!/bin/bash

echo "runnr;alertLevel" >alert.csv

start=35130
end=35139

for run in $(seq $start $end)
do
    max=$(./build/HV-quality-first-filter $run 2>/dev/null \
        | grep -P '#     Max:' \
        | sed 's/.*Max: //')
    echo $run $max
    if [ $max != 0 ]
    then
        echo "$run;$max" >>alert.csv
    fi
done
```

Table Ak: **HV anomalies during commissioning measurements with gaseous $^{83\mathrm{m}}$Kr.** The alert level value is a return value of the high voltage quality filter (see section 6.1). The run number corresponds to the FPD run, during which the anomaly occured. Details to the anomaly types can be found in chapter 6.

anomaly type	alert level	list of runs with anomaly
missing sensor reading (calibration)	100	33096
missing sensor reading (sensor error)	100	33089, 33239, 33261, 33265, 33188
drop to zero	50, 100	33172, 33173
peak at voltage step	10, 50	33048, 33061, 33069, 33070, 33071, 33194, 33241, 33247, 33248, 33249, 33250, 33251, 33252, 33253, 33254, 33255

Table AI: **HV anomalies during commissioning measurements with condensed $^{83\mathrm{m}}$Kr.** The alert level value is a return value of the high voltage quality filter (see section 6.1). The run number corresponds to the FPD run, during which the anomaly occured. Details to the anomaly types can be found in chapter 6.

anomaly type	alert level	list of runs with anomaly
missing sensor reading (calibration)	100	33313
missing sensor reading (sensor error)	100	33288, 33293, 33302, 33305, 33309, 33349, 33445, 33481, 33489, 33495, 33497, 33509, 33567, 33576
drop to zero	50	33522
peak at voltage step	10, 50	33468, 33477, 33487, 33504, 33514, 33531, 33541

Table Am: **HV anomalies during spectrometer commissioning measurements.** Here an excerpt of runs with voltage anomalies during the measurement phase, beginning in August, 2017 up to the end of September, 2017 is listed. The alert level value is a return value of the high voltage quality filter (see section 6.1). The run number corresponds to the FPD run, during which the anomaly occured. Details to the anomaly types can be found in chapter 6.

anomaly type	alert level	list of runs with anomaly
missing sensor reading (calibration)	100	33858, 33960, 34147, 34149, 34254, 34400, 34401, 34402, 34438, 34439, 34466, 34483, 34498
missing sensor reading (sensor error)	100	33710, 33723, 33728, 33752, 33753, 33788, 33803, 33810, 33813, 33826, 33834, 33839, 33864, 33869, 33898, 33909, 33931, 33988, 34036, 34076, 34084, 34086, 34087, 34117, 34148, 34223, 34237, 34252, 34272, 34273, 34321, 34378, 34406, 34407, 34409, 34410, 34412, 34418, 34472, 34473, 34476, 34479, 34481, 34484, 34486
drop to zero	50, 100	33815, 34073, 34270, 34271, 34414, 34421

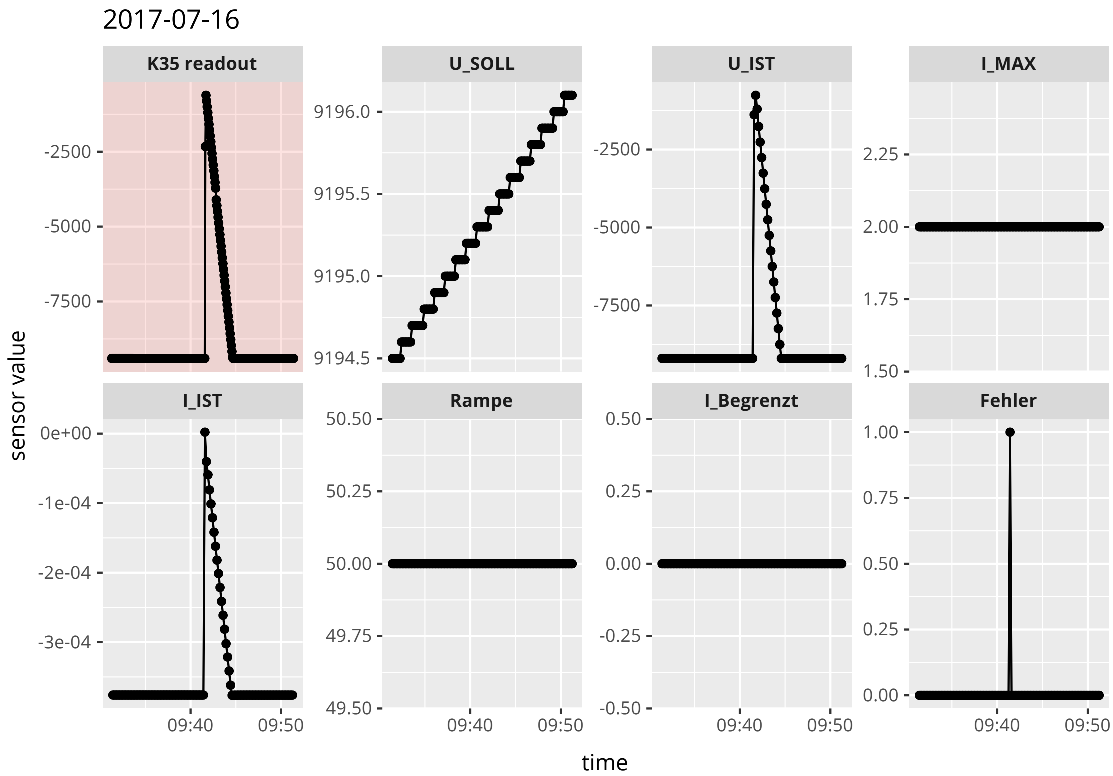

Figure An: **Example of a sudden voltage drop to almost zero.** The plot in the upper left, marked in red shows the voltage reading with DVM-A. The other seven plots show sensor readings of the precision power supply over time. One can see that the voltage drop coincides with drops in other values. In table 4a in section 4.1.1 the mapping between the ADEI sensor identifications used in the plot is listed.

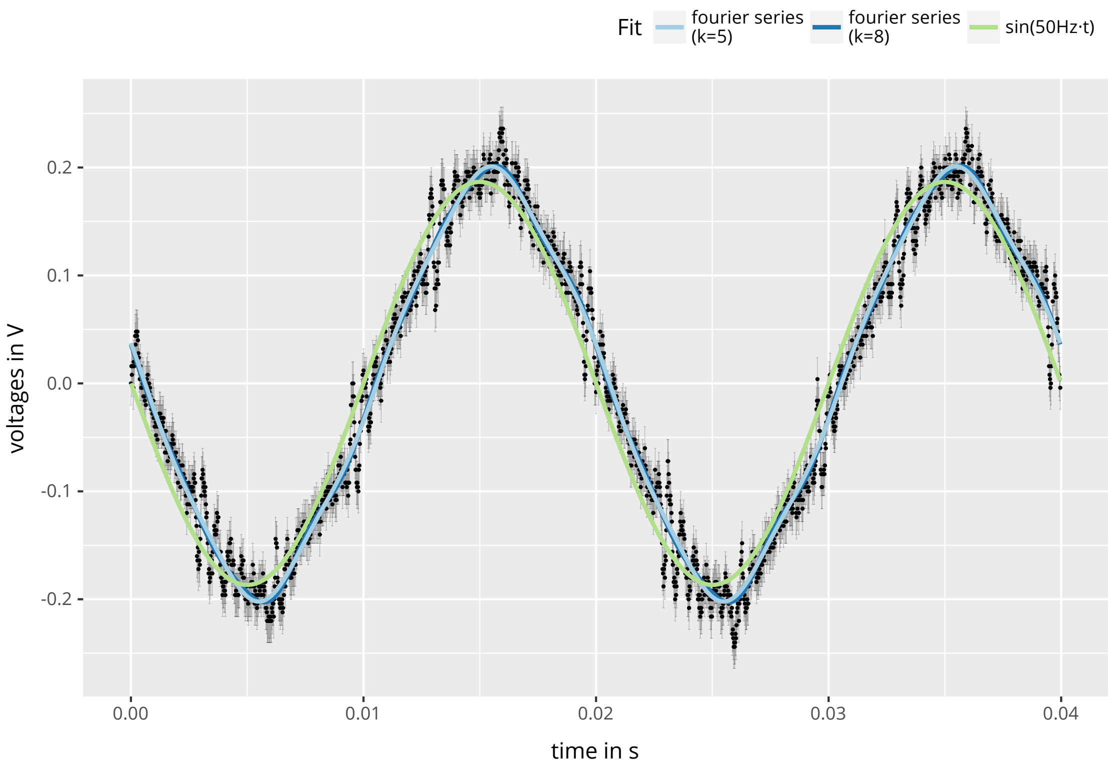

Figure Ao: **Ripple-Probe readout with oscilloscope at 17 kV, measurement A.** The black dots are the voltage values read from the oscilloscope. The error bars represent an error for every voltage point of ± 10 mV. The three lines show different fits applied on the oscilloscope data.

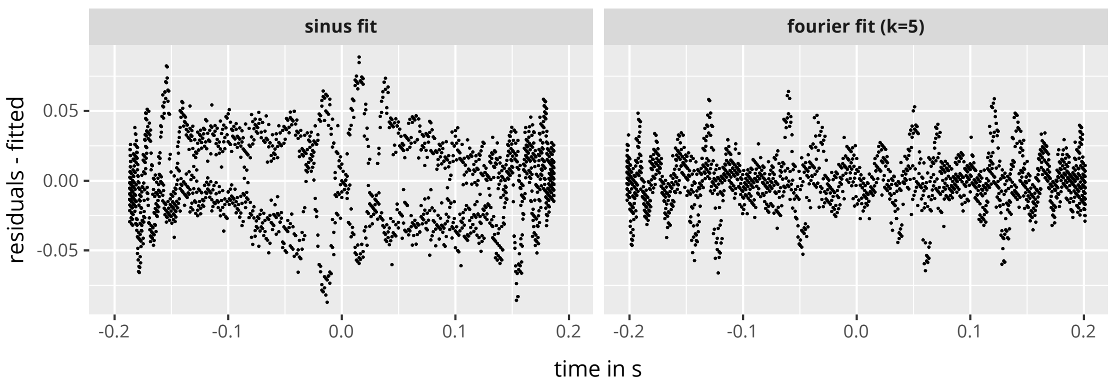

Figure Ap: **Residuals for fits on oscilloscope readout at 17 kV, measurement A.** The left plot shows the residuals plotted against the fitted values of the sinusoidal fit shown in figure Ar. The right plot is the same for the fit with a Fourier base with $k = 5$.

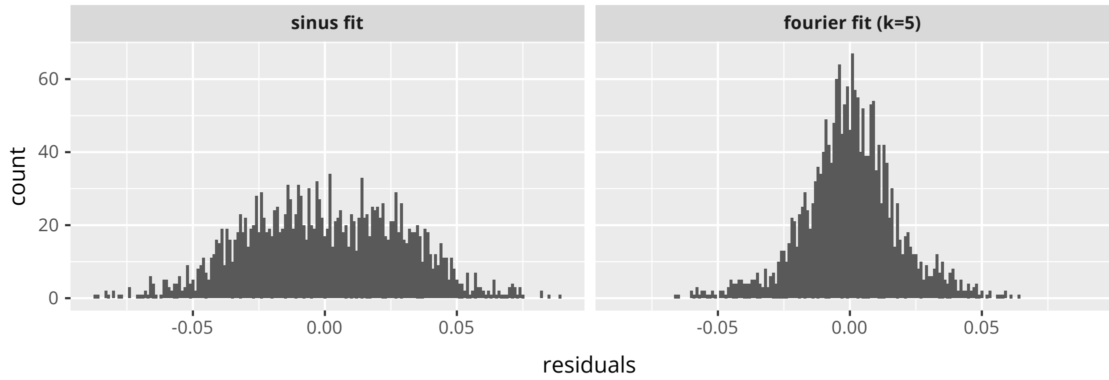

Figure Aq: **Histogram of residuals for fits on oscilloscope readout at 17 kV, measurement A.** The left plot shows a histogram of the residuals plotted against the fitted values of the sinusoidal fit shown in figure Ao. The right plot is the same for the fit with a Fourier base with $k = 5$. A Gaussian fit for this histogram gives a standard deviation of 0.0297 V for the sine fit, and 0.0180 V for the Fourier base fit.

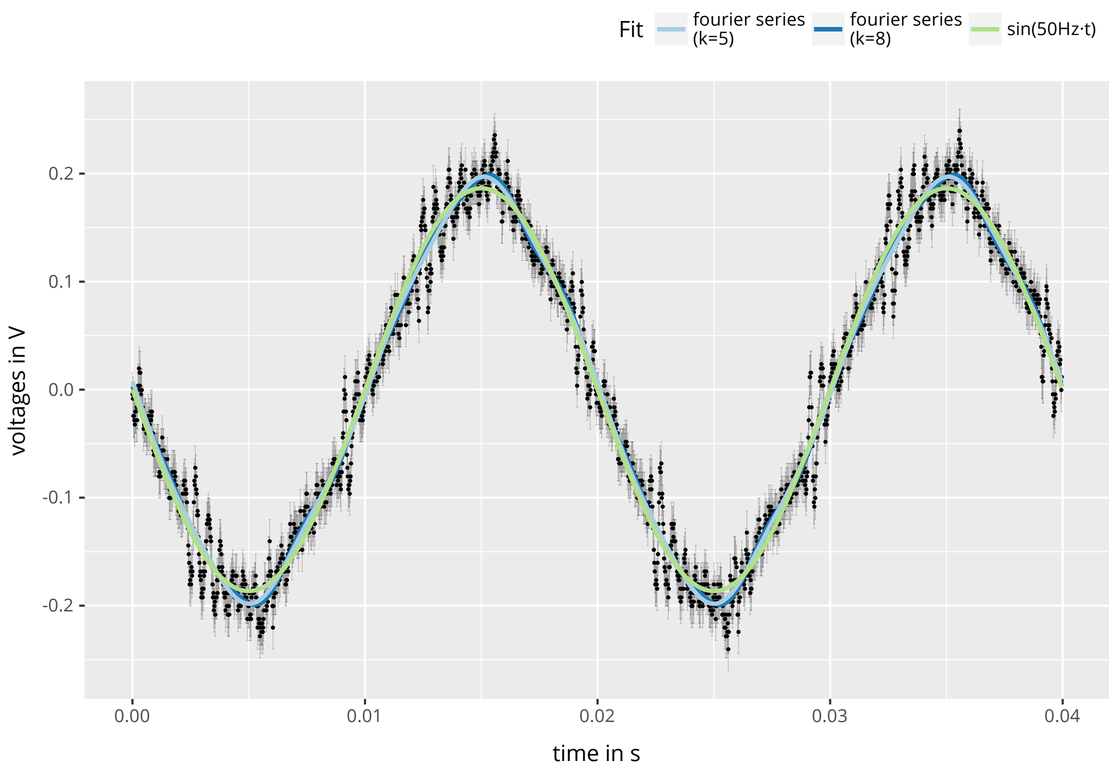

Figure Ar: **Ripple-Probe readout with oscilloscope at 17 kV, measurement B.** The black dots are the voltage values read from the oscilloscope. The error bars represent an error for every voltage point of ±10 mV. The three lines show different fits applied on the oscilloscope data.

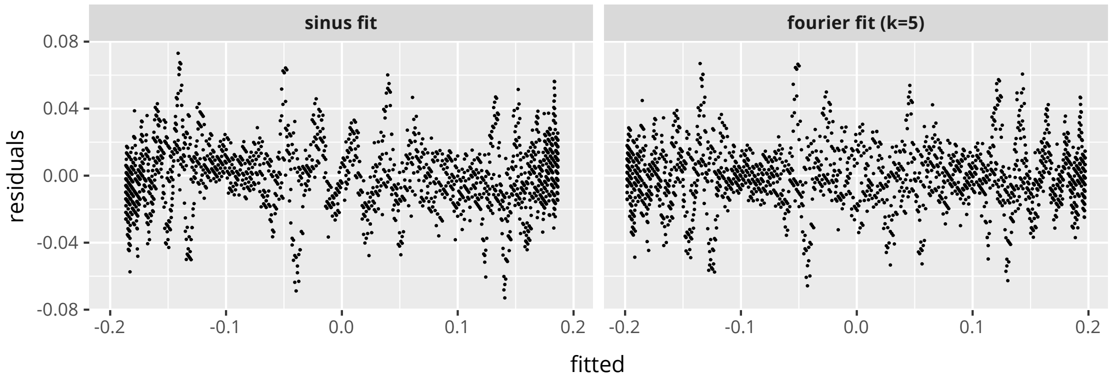

Figure As: **Residuals for fits on oscilloscope readout at 17 kV, measurement B.** The left plot shows the residuals plotted against the fitted values of the sinusoidal fit shown in figure Ar. The right plot is the same for the fit with a Fourier base with $k = 5$.

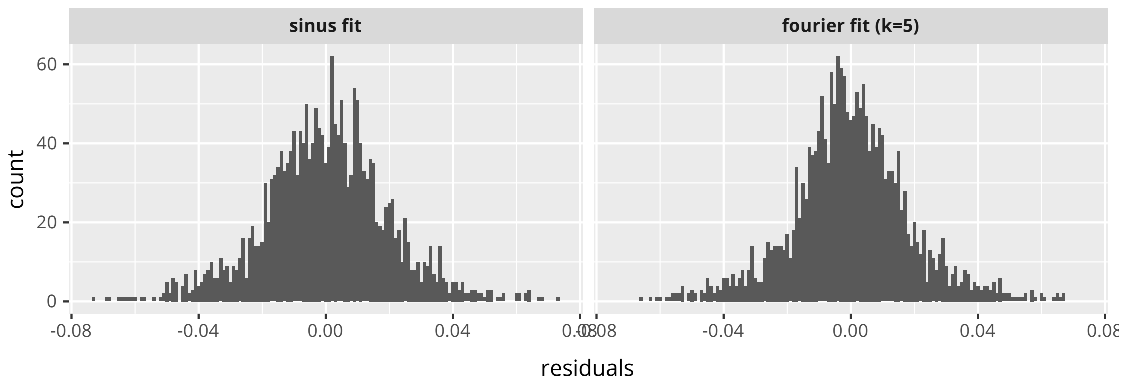

Figure At: **Histogram of residuals for fits on oscilloscope readout at 17 kV, measurement B.** The left plot shows a histogram of the residuals plotted against the fitted values of the sinusoidal fit shown in figure Ar. The right plot is the same for the fit with a Fourier base with $k = 5$. A Gaussian fit for this histogram gives a standard deviation of 0.0198 V for the sine fit, and 0.0187 V for the Fourier base fit.

Bibliography

ADE, P. A. R. et al., 2014. Planck 2013 results. XVI. Cosmological parameters. *A&A*. 2014. Vol. 571, p. A16. DOI 10.1051/0004-6361/201321591.

AGAFONOVA, N. et al., 2015. Discovery of τ Neutrino Appearance in the CNGS Neutrino Beam with the OPERA Experiment. *Phys. Rev. Lett.* September 2015. Vol. 115, no. 12, p. 121802. DOI 10.1103/PhysRevLett.115.121802.

AGOSTINI, M. et al., 2013. Results on Neutrinoless Double-β Decay of ^{76}Ge from Phase I of the GERDA Experiment. *Phys. Rev. Lett.* September 2013. Vol. 111, no. 12, p. 122503. DOI 10.1103/PhysRevLett.111.122503.

AHMAD, Q. R. et al., 2001. Measurement of the Rate of $\nu_e + d \rightarrow p + p + e^-$ Interactions Produced by ^8B Solar Neutrinos at the Sudbury Neutrino Observatory. *Phys. Rev. Lett.* July 2001. Vol. 87, no. 7, p. 071301. DOI 10.1103/PhysRevLett.87.071301.

ALTARELLI, Guido [Hrsg.] (ed.), 2003. Laboratory Limits on Neutrino Masses. In: *Neutrino mass*. Berlin: Springer. ISBN 3-540-40328-0.

AMSBAUGH, J. F. et al., 2015. Focal-plane detector system for the KATRIN experiment. *Nuclear Instruments and Methods in Physics Research Section A: Accelerators, Spectrometers, Detectors and Associated Equipment*. 1 April 2015. Vol. 778, p. 40–60. DOI 10.1016/j.nima.2014.12.116.

ANDREOTTI, E. et al., 2007. MARE, Microcalorimeter Arrays for a Rhenium Experiment: A detector overview. *Nuclear Instruments and Methods in Physics Research Section A: Accelerators, Spectrometers, Detectors and Associated Equipment*. 1 March 2007. Vol. 572, no. 1, p. 208–210.

ANGRIK, J. et al., 2005. *KATRIN design report 2004*. Karlsruhe: Forschungszentrum Karlsruhe.

ARAKI, T. et al., 2005. Experimental investigation of geologically produced antineutrinos with KamLAND. *Nature*. 28 July 2005. Vol. 436, p. 499 EP. DOI 10.1038/nature03980.

ARENZ, M. et al., 2016. Commissioning of the vacuum system of the KATRIN Main Spectrometer. *Journal of Instrumentation*. 2016. Vol. 11, no. 04, p. P04011. DOI 10.1088/1748-0221/11/04/P04011.

ARENZ, M. et al., 2018a. First transmission of electrons and ions through the KATRIN beamline. [online]. 2018. Available from: https://arxiv.org/abs/1802.04167

ARENZ, M. et al., 2018b. Calibration of high voltages at the ppm level by the difference of ^{83m}Kr conversion electron lines at the KATRIN experiment.. 2018.
arxive:submit2162559 [physics.ins.-det] 13 Feb 2018

ASEEV, V. N. et al., 2011. Upper limit on the electron antineutrino mass from the Troitsk experiment. *Phys. Rev. D*. December 2011. Vol. 84, no. 11, p. 112003. DOI 10.1103/PhysRevD.84.112003.

BABUTZKA, M et al., 2012. Monitoring of the operating parameters of the KATRIN Windowless Gaseous Tritium Source. *New Journal of Physics*. 2012. Vol. 14, no. 10, p. 103046. DOI 10.1088/1367-2630/14/10/103046.

BAUER, S. et al., 2013. Next generation KATRIN high precision voltage divider for voltages up to 65kV. *Journal of Instrumentation*. 2013. Vol. 8, no. 10, p. P10026. DOI 10.1088/1748-0221/8/10/P10026.

BEAMSON, G et al., 1980. The collimating and magnifying properties of a superconducting field photoelectron spectrometer. *Journal of Physics E: Scientific Instruments*. 1980. Vol. 13, no. 1, p. 64. DOI 10.1088/0022-3735/13/1/018.

BEHRENS, Jan, 2017. *Issues with PCH / DET current readouts* [online]. Electronic Logbook Entry. September 2017. Available from: https://neutrino.ikp.kit.edu:8080/KryptonJuly17/105

CHILINGARYAN, S. et al., 2010. Advanced data extraction infrastructure: Web based system for management of time series data. *Journal of Physics: Conference Series*. 2010. Vol. 219, no. 4, p. 042034. DOI 10.1088/1742-6596/219/4/042034.

COWAN, C. L. et al., 1956. Detection of the Free Neutrino: a Confirmation. *Science*. 1956. Vol. 124, no. 3212, p. 103–104. DOI 10.1126/science.124.3212.103.

DANBY, G. et al., 1962. Observation of High-Energy Neutrino Reactions and the Existence of Two Kinds of Neutrinos. *Phys. Rev. Lett.* July 1962. Vol. 9, no. 1, p. 36–44. DOI 10.1103/PhysRevLett.9.36.

DAVIS, Raymond, Jr., 1964. Solar neutrinos. ii. experimental. *Physical Review Letters*. 1964. Vol. 12, no. 11, p. 303.

DRAGOUN, O. et al., 2004. Increased Accuracy of the Binding Energy of K- and L-Subshell Electrons in Krypton from Re-analysis of Experimental Data: Importance for Determination of the Neutrino Mass. *Czechoslovak Journal of Physics*. 1 August 2004. Vol. 54, no. 8, p. 833–839. DOI 10.1023/B:CJOP.0000038591.13369.e1.

ELLIOTT, S. R. et al., 1987. Direct evidence for two-neutrino double-beta decay in ^{82}Se. *Phys. Rev. Lett.* November 1987. Vol. 59, no. 18, p. 2020–2023. DOI 10.1103/PhysRevLett.59.2020.

ENOMOTO, S., 2017a. *BEANS First Step* [online]. June 2017. Available from: http://katana.npl.washington.edu/∼sanshiro/BeansTutorial/20170628/BeansFirstStep.pdf

ENOMOTO, S., 2017b. *BEANS for Krypton-Mode Measurement* [online]. June 2017. Available from: http://katana.npl.washington.edu/∼sanshiro/BeansTutorial/20170628/KryptonBeans.pdf

ERHARD, M et al., 2014. High-voltage monitoring with a solenoid retarding spectrometer at the KATRIN experiment. *Journal of Instrumentation*. 2014. Vol. 9, no. 06, p. P06022. DOI 10.1088/1748-0221/9/06/P06022.

EVSLIN, Jarah et al., 2016. The leptonic CP phase from T2(H)K and $\mu+$ decay at rest. *Journal of High Energy Physics*. 22 February 2016. Vol. 2016, no. 2, p. 137. DOI 10.1007/JHEP02(2016)137.

FERMI, E., 1934. Versuch einer Theorie der β-Strahlen. I. *Zeitschrift für Physik*. 1 March 1934. Vol. 88, no. 3, p. 161–177. DOI 10.1007/BF01351864.

FLUKE, Calibration, 1983. *732B/734A DC Reference Standard*. May 1983. John Fluke Mfg. Co., Inc.

FLUKE, Calibration, 2002. *8508A Reference Multimeter Users Manual*. 2002. Rev. 6, 3/13. Fluke Corporation.

FLUKE, Calibration, 2012. *732B/734A DC Reference Standard*. August 2012. Fluke Corporation.

FRÄNKLE, F. M. et al., 2011. Radon induced background processes in the KATRIN pre-spectrometer. *Astroparticle Physics*. October 2011. Vol. 35, p. 128–134. DOI 10.1016/j.astropartphys.2011.06.009.

FUG, 2008a. *High Voltage Power Supplies HCP - Series*. 2008. FuG Elektronik GmbH.

FUG, 2008b. *Hochspannungs - Netzgeräte HCN - Serie*. 2008. FuG Elektronik GmbH.

FUKUDA, Y. et al., 1998. Evidence for Oscillation of Atmospheric Neutrinos. *Phys. Rev. Lett.* August 1998. Vol. 81, no. 8, p. 1562–1567. DOI 10.1103/PhysRevLett.81.1562.

GASTALDO, L. et al., 2014. The Electron Capture ^{163}Ho Experiment ECHo. *Journal of Low Temperature Physics*. 1 September 2014. Vol. 176, no. 5, p. 876–884. DOI 10.1007/s10909-014-1187-4.

GLASHOW, Sheldon L., 1961. Partial-symmetries of weak interactions. *Nuclear Physics*. 1961. Vol. 22, no. 4, p. 579–588. DOI https://doi.org/10.1016/0029-5582(61)90469-2.

GOEPPERT-MAYER, M., 1935. Double Beta-Disintegration. *Phys. Rev.* September 1935. Vol. 48, no. 6, p. 512–516. DOI 10.1103/PhysRev.48.512.

GRIFFITHS, David J., 2008. *Introduction to elementary particles*. 2., rev. ed. Weinheim: Wiley-VCH. Physics textbook. ISBN 3-527-40601-8; 978-3-527-40601-2.

Guide to the expression of uncertainty in measurement, 1993.. 1. ed. Genève: Bureau International des Poids et Mesures; International Organization for Standardization. ISBN 92-67-10188-9.

JOSEPHSON, B. D., 1962. Possible new effects in superconductive tunnelling. *Physics Letters*. 1962. Vol. 1, no. 7, p. 251–253. DOI 10.1016/0031-9163(62)91369-0.

KODAMA, K. et al., 2001. Observation of tau neutrino interactions. *Physics Letters B*. 2001. Vol. 504, no. 3, p. 218–224. DOI https://doi.org/10.1016/S0370-2693(01)00307-0.

KOSMIDER, Andreas, 2012. *Tritium Retention Techniques in the KATRIN Transport Section and Commissioning of its DPS2-F Cryostat* [online]. Dissertation. Karlsruhe. Available from: http://nbn-resolving.org/urn:nbn:de:swb:90-289595

KOSMIDER, Andreas, 2015. *The Cryogenic Pumping Section of the KATRIN Experiment - Design Studies and Experiments for the Commissioning* [online]. Dissertation. Karlsruhe. Available from: http://nbn-resolving.org/urn:nbn:de:swb:90-471467

KRAUS, Ch et al., 2005. Final results from phase II of the Mainz neutrino mass search in tritium β decay. *The European Physical Journal C - Particles and Fields*. 1 April 2005. Vol. 40, no. 4, p. 447–468. DOI 10.1140/epjc/s2005-02139-7.

KRAUS, Marcel, 2016. *Energy-scale systematics at the KATRIN main spectrometer*. Dissertation. Karlsruhe.

LEFHALM, C. H. and KRIEGER, V., 2005. A full featured monitoring, control and data management system for liquid metal coolant loops. *14th IEEE-NPSS Real Time Conference.* 2005. P. 4ff. DOI 10.1109/RTC.2005.1547521.

LOBASHEV, V. M. et al., 1985. A method for measuring the electron antineutrino rest mass. *Nuclear Instruments and Methods in Physics Research Section A: Accelerators, Spectrometers, Detectors and Associated Equipment*. 15 October 1985. Vol. 240, no. 2, p. 305–310. DOI 10.1016/0168-9002(85)90640-0.

LUKIĆ, S. et al., 2012. Measurement of the gas-flow reduction factor of the KATRIN DPS2-F differential pumping section. *Vacuum*. 2012. Vol. 86, no. 8, p. 1126–1133. DOI 10.1016/j.vacuum.2011.10.017.

MACHATSCHEK, Moritz, 2016. *Simulation of the 83m Kr Mode of the Tritium Source of the KATRIN Experiment* [online]. 2016. Available from: http://www.katrin.kit.edu/publikationen/mth_Schimpf.compressed.pdf

MAJORANA, E., 1937. Teoria simmetrica dell'elettrone e del positrone. *Il Nuovo Cimento*. April 1937. Vol. 14, p. 171–184. DOI 10.1007/BF02961314.

MAKI, Ziro et al., 1962. Remarks on the Unified Model of Elementary Particles. *Progress of Theoretical Physics*. 1 November 1962. Vol. 28, no. 5, p. 870–880. DOI 10.1143/PTP.28.870.

MCCUTCHAN, E. A., 2015. Nuclear Data Sheets for A = 83. *Nuclear Data Sheets*. 1 March 2015. Vol. 125, p. 201–394. DOI 10.1016/j.nds.2015.02.002.

PATRIGNANI, C. et al., 2016. Review of Particle Physics. *Chin. Phys.* 2016. Vol. C40, no. 10, p. 100001. DOI 10.1088/1674-1137/40/10/100001.

PAULI, Wolfgang, 1930. *Offener Brief an die Gruppe der Radioaktiven bei der Gauverein-Tagung zu Tübingen.* 1930.

PERKINS, Donald H., 2009. *Particle astrophysics*. 2. ed. Oxford: Oxford University Press. Oxford master series in physics ; no. 10. ISBN 978-0-19-954546-9.

PICARD, A. et al., 1992. A solenoid retarding spectrometer with high resolution and transmission for keV electrons. *Nuclear Instruments and Methods in Physics Research Section B: Beam Interactions with Materials and Atoms*. 1 February 1992. Vol. 63, no. 3, p. 345–358. DOI 10.1016/0168-583X(92)95119-C.

PICARD, A. et al., 1992. Precision measurement of the conversion electron spectrum of $^{83\mathrm{m}}Kr$ with a solenoid retarding spectrometer. *Zeitschrift für Physik A Hadrons and Nuclei*. 1 March 1992. Vol. 342, no. 1, p. 71–78. DOI 10.1007/BF01294491.

PONTECORVO, B., 1968. Neutrino Experiments and the Problem of Conservation of Leptonic Charge. *Soviet Journal of Experimental and Theoretical Physics*. May 1968. Vol. 26, p. 984.

PRALL, Matthias, 2011. *Background Reduction of the KATRIN Spectrometers: Transmission Function of the Pre-Spectrometer and Systematic Tests of the Main-Spectrometer Wire Electrode*. Dissertation. Münster.

PRIESTER, Florian et al., 2015. Commissioning and detailed results of KATRIN inner loop tritium processing system at Tritium Laboratory Karlsruhe. *Vacuum*. 2015. Vol. 116, p. 42–47. DOI 10.1016/j.vacuum.2015.02.030.

REST, Oliver, 2014. *Inbetriebnahme der Präzisionshochspannung am Hauptspektrometer des KATRIN-Experiments* [online]. 2014. Available from: http://www.uni-muenster.de/Physik.KP/AGWeinheimer/Files/theses/master_oliver_rest.pdf

REST, Oliver, 2018. *Dissertation in preperation.* 2018.

SALAM, A., 1968. *Elementary particle theory: Relativistic groups and analyticity. Proccedings of the Eighth Nobel Symposium held May 19-25, 1968 at Aspenäsgarden, Lerum, in the county of Älvsborg, Sweden*. Almqvist & Wiksell. Nobel symposium.

SCHIMPF, Lutz, 2017. *Studies on thermal and radioactive impacts on the tritium retention of the cryogenic pumping section of KATRIN* [online]. 2017. Available from: http://www.katrin.

kit.edu/publikationen/mth_Schimpf.compressed.pdf

SCHMIDT, Matthias and MEISNER, Johann, 2013. 1K-23009: *Überprüfung des Hochspannungsteilers KT 35*. Physikalisch-Technische Bundesanstalt.

SCHMITZ, Norbert, 1997. *Neutrinophysik : mit 23 Tabellen*. Stuttgart: Teubner. Teubner-Studienbücher : Physik. ISBN 3-519-03236-8.

SHAPIRO, Sidney, 1963. Josephson Currents in Superconducting Tunneling: The Effect of Microwaves and Other Observations. *Phys. Rev. Lett.* July 1963. Vol. 11, no. 2, p. 80–82. DOI 10.1103/PhysRevLett.11.80.

THÜMMLER, Th. et al., 2009. Precision high voltage divider for the KATRIN experiment. *New Journal of Physics*. 2009. Vol. 11, no. 10, p. 103007. DOI 10.1088/1367-2630/11/10/103007.

THÜMMLER, Thomas, 2007. *Präzisionsüberwachung und Kalibration der Hochspannung für das KATRIN-Experiment* [online]. Dissertation. Münster. Available from: http://www.uni-muenster.de/Physik.KP/AGWeinheimer/Files/theses/Diplom_Thomas_Thuemmler.pdf

WEINBERG, Steven, 1967. A Model of Leptons. *Phys. Rev. Lett.* November 1967. Vol. 19, no. 21, p. 1264–1266. DOI 10.1103/PhysRevLett.19.1264.

ZBOŘIL, M et al., 2013. Ultra-stable implanted ^{83}Rb/ ^{83m}Kr electron sources for the energy scale monitoring in the KATRIN experiment. *Journal of Instrumentation*. 2013. Vol. 8, no. 03, p. P03009. DOI 10.1088/1748-0221/8/03/P03009.

Danksagung

Mein Dank geht an all jene, die es mir ermöglicht haben, diese Masterarbeit zu schreiben.

Insbesondere möchte ich mich bei Professor Guido Drexlin bedanken für die Möglichkeit am KATRIN-Experiment die Masterarbeit zu schreiben.

Bei meiner Korreferentin Kathrin Valerius möchte ich mich für ihre stete Hilfsbereitschaft und für das Schaffen einer schönen Arbeitsatmosphäre bedanken.

Für die tolle Betreuung während der gesamten Zeit der Masterarbeit bedanke ich mich ganz herzlich bei Thomas Thümmler, der jederzeit ein offenes Ohr für Fragen zu allen Themen hatte. Die vielen lehrreichen Diskussionen und das Korrekturlesen haben wesentlich zum Gelingen dieser Masterarbeit beigetragen.

Ebenso geht mein Dank an Moritz Erhard, der am Anfang meiner Masterarbeit mir Vieles zum KATRIN-Experiment erklärt hat und mir den Einstieg in die Masterarbeit leicht gemacht hat.

Bei Oliver Rest möchte ich mich bedanken für die spannenden Messphasen, bei denen ich sehr viel über das Hochspannungssystem lernen konnte. Auch hat er sich immer Zeit genommen für Fragen aller Art.

Sascha Wüstling möchte ich danken für seine Antworten und Hilfen zu allen Fragen zum Hochspannungssystem und der Elektrotechnik im Allgemeinen.

Für die sorgsamen und zuverlässig durchgeführten Kalibrierungen möchte ich mich bei Heike Bolz bedanken. Ohne ihr Engagement wäre die Kalibrierungs-Historie nicht so kontinuierlich gewesen, wie sie es jetzt ist.

Für die sehr lehrreiche Zeit am Monitorspektrometer möchte ich mich bei Klaus Schlösser bedanken.

I want to thank Sanshiro Enomoto for his detailed explanations about BEANS and Fourier analysis.

Florian Fränkle, Philipp Ranitzsch und Jan Behrens möchte ich danken dafür, dass sie immer bei allen möglichen physikalischen und organisatorischen Fragen Rat wussten.

Ebenso möchte ich mich bei der gesamten KATRIN-Arbeitsgruppe bedanken für die sehr schöne Arbeitsatmosphäre und für all die hilfreichen und unterhaltsamen Gespräche. Für die tagtäglich geregelt einberufenen Mittagspausen in netter Atmosphäre möchte ich mich bei Klaus Mehret bedanken.

Ganz besonders bedanken möchte ich mich bei meiner Familie und bei Christopher. Vor allem mit eurer stetigen Unterstützung und eurer Geduld mit mir, auch in den etwas stressigeren Phasen und ebenso mit dem sprachlichen Feinschliff dieser Masterarbeit durch Christopher und meine Schwester Christine, habt ihr zum Gelingen beigetragen.